Contents lists available at ScienceDirect

Materials Characterization

Microstructure evolution in the context of fracture in austenitic steels under complex loads at cryogenic temperatures

Kinga Nalepka [a,*], Błażej Skoczeń [b], Rafał Schmidt [b], Marlena Ciepielowska [b], Elwira Schmidt [b], Robert Chulist [c]

[a] Faculty of Mechanical Engineering and Robotics, AGH University of Science and Technology, 30-059 Kraków, Poland
[b] Faculty of Mechanical Engineering, Cracow University of Technology, 31-155 Kraków, Poland
[c] Institute of Metallurgy and Materials Science, Polish Academy of Sciences, 30-059 Kraków, Poland

ARTICLE INFO

ABSTRACT

The microstructure evolution and its coupling with fracture under complex load conditions at the temperature of liquid helium are investigated. Tension combined with torsion was applied to thin-walled cylindrical samples made of AISI 304 steel. The second component load is the key. The torque causes the sample to buckle, and the resulting folds and wells differentiate the conditions in which the transformation occurs. The feritoscopic examinations combined with the profilometer surface characterization revealed that martensite α' initiates in the slopes of elevations, where the highest shear stresses arise. The secondary phase has a special cross-lamellar microstructure, uncovered in detailed studies using the electron backscatter diffraction (EBSD) method and synchrotron X-ray diffraction. The new phase prefers the transverse direction of the cylinder surface, which remains invariant during torsion. Along it, the martensite α' grain develops, which then twins so as to continue growing along the second plane of the maximum shear stresses. In the advanced stage of the phase transformation, the resulting martensite α' has compact microstructure able to block fracture propagation and to deflect its path. The macrocrack trajectory and the secondary phase distribution coupled with it were reconstructed with high accuracy in the extended finite element method (XFEM) simulation.

1. Introduction

The continuous development of technology, stimulated by the growing needs of civilization, means that more and more machines and devices work in cryogenic conditions. Structures and instrumentation, such as particle accelerators, spaceships or the magnetic trains (maglev) requiring extremely low temperatures, are usually made of stainless steel grades 304, 304L, 316, 316L, 316Ti, 321 etc [1–3]. These materials show excellent mechanical properties, including high strength and ductility, based on transformation induced plasticity (TRIP) [4–6]. The phase transformation of the plastic matrix formed by austenite with a face centered cubic (fcc) structure generates harder martensite α' inclusions with a body centered cubic structure (bcc) [7,8]. This process strengthens the material under operating conditions, but is also involved in the initiation and propagation of the fracture in a failure situation. The phase transformation induces a local strain determined by the Bain tensor [9]. The formation of the bcc martensite α' structure from the fcc

austenitic one entails an increase in the volume per atom and a shape change. The basic model that effectively describes the experimentally observed phase transformation was developed by Bogers and Burgers [10]. According to it, martensite α' is formed at the intersection of two shear bands. They are generated by displacements $\frac{a_{fcc}}{12}[1\,\overline{1}\,\overline{2}]_\gamma$ and $\frac{a_{fcc}}{18}[\overline{1}\,1\,\overline{2}]_\gamma$ constituting respectively the second ($T/2$) and the third ($T/3$) part of the twin shear $T = \frac{a_{fcc}}{6}\langle 1\,1\,2\rangle_\gamma$. The first of them takes place in the subsequent planes $(\overline{1}\,1\,1)_\gamma$ and the second in the system of planes $(1\,\overline{1}\,\overline{1})_\gamma$. Olson and Cohen [11] indicated that the source of the $T/2$ shear may be a partial Shockley dislocation spreading over two planes $(\overline{1}\,1\,\overline{1})_\gamma$. This process leads to the creation of an ideal martensite plate ε with a hexagonal structure. Likewise, $T/3$ shear is derived from a partial dislocation spreading over three adjacent planes $(1\,\overline{1}\,\overline{1})_\gamma$. This time, the resulting structure is not hexagonal close packed. Nevertheless, high-resolution microscopy studies revealed that the dislocations of the shear $T/3$ come from the second martensite lath ε[12]. After the

---

formation of the martensite α' island unused dislocations cause, inside the second martensite plate ε, local retransformation to phase γ. Finally, the martensite α' formed preserves the well-known relationship of the Kurdjumov–Sachs orientation with the austenitic matrix. During tension, the martensite α' nucleus grows along the $T/2$ shear band due to the large deformation [13]. The presented model of nucleation was used by Olson and Cohen to develop the kinetics of strain-induced phase transformation. The obtained dependence of the martensite α' volume fraction on plastic deformation became the basis for building subsequent models [14]. They take into account the more and more precise characteristics of the phase transformation revealed in a number of experimental studies conducted. The developed kinetics combine the plastic strain-induced transformation with the stress-assisted one and predict the volume fraction of not only martensite α' but also martensite ε or mechanical twins [15]. It is also worth paying attention to the crystallographic modification of the Olson-Cohen kinetics proposed by M. Zecevic et al. [16]. The authors created a crystal plasticity model based on the local stress state, treating the resolved shear stress as a factor that determines the potential sites of martensite α' nucleation.

The aim of the work is to investigate the growth of martensite α' and the coupling of this process with the crack propagation in 304 grade stainless steel subjected to a complex load at the temperature of liquid helium. Tests of tension combined with torsion were carried out on thin-walled cylindrical samples. Investigations by the EBSD method and the X-ray diffraction technique using synchrotron radiation, performed before the initiation of the macrocrack and after the specimen rupture, enables a detailed study of the microstructure evolution. The use of torsion has a particular effect on the initiation and growth of martensite α'. This load induces plane shear in the cylinder wall. Thus, in the transverse direction, a material invariant fiber is formed. Its presence is crucial for the two known paths of phase transformation the Kurdjumov–Sachs and Pitsch. The relationship of the invariant fiber with the initiation and growth of martensite α' was analyzed in detail during the conducted research. The action of the torsional moment leads to the additional effect of buckling of a thin-walled cylindrical sample. The resulting bending states, folds and wells differentiate the conditions of the phase transformation, which allows to study the factors controlling the initiation and growth of martensite α'. The connection of the secondary phase distribution with the surface topography of the sample, which locally has lost its stability, was obtained by performing investigations with the use of a feritscope and a non-contact profilometer. The results of the conducted studies became the basis for the identification of interactions between the emerging martensite α' fields and the macrocrack development.

1.1. Lattice excitation at extremely low temperatures

Lattice excitation is function of temperature. When decreasing the temperature from room temperature down to absolute zero, the amount of thermal energy decreases to reach 0 at the temperature of absolute zero. This is due to the 3rd law of thermodynamics (the Nernst principle) that states that the entropy tends to 0 with temperature. This has direct impact on the behavior of lattice and determines the thermodynamic functions, including the specific heat, the thermal conductivity and the thermal contraction coefficient. As the thermal energy stored in the lattice is sum of two components: the energy of phonons and the energy related to free electrons (the Fermi gas), the specific heat can be computed in the form of derivative of the energy with respect to temperature. Taking into account the phonon mechanism, the energy of the quantum lattice vibrations reads [17]:

$$E_{ph} \sim NT^4\theta^{-3} \tag{1}$$

where N denotes the number of atoms (cells) in the lattice, T is the temperature, and θ is the normalized reference temperature. The specific

heat (at constant volume) is obtained by differentiating the above term with respect to temperature:

$$(C_{ph})_V = \partial_T E_{ph}|_V \sim NT^3\theta^{-3} \tag{2}$$

The contribution of free electrons to the specific heat is expressed by:

$$(C_{el})_V \sim TT_F^{-1} \tag{3}$$

where T_F denotes the Fermi reference temperature. Finally, the specific heat reads:

$$C_V = (C_{el})_V + (C_{ph})_V \sim TT_F^{-1} + NT^3\theta^{-3} \tag{4}$$

Computing the heat increment and the derivative of temperature with respect to heat, one obtains:

$$dQ = mC_V dT \quad ; \quad dT/dQ = (mC_V)^{-1} \tag{5}$$

which implies the following conclusion:

$$C_V|_{T\to 0}\to 0 \quad ; \quad dT/dQ\to\infty \tag{6}$$

This is crucial for extremely low temperatures since the specific heat tending to zero with temperature implies the derivative of temperature with respect to heat tending to infinity. This means that any arbitrarily small increment of heat deposited in the lattice under the adiabatic conditions will produce a temperature rise in the form of the Dirac function. This has an important impact on the thermomechanical coupling affecting such phenomena, like the intermittent plastic flow.

1.2. Low temperature plasticity and fracture

In the light of thermodynamics described in the previous section, the inelastic behavior of ductile materials at extremely low temperatures differs from what is observed at room and at enhanced temperatures because of the lack of thermal energy in the lattice [18]. In particular, low temperature plasticity is determined mainly by the conditions of dislocations motion in the lattice. As already stated, in the proximity of absolute zero lattice is weakly excited which implies lack of thermal energy and apparent domination of edge dislocations over screw dislocations. As the edge dislocations do not easily overcome the obstacles, especially that the thermal energy stored in the lattice is low, they pile up on the lattice barriers forming groups characterized by increasing shear stress at the head of the pile-up. With the increasing load, the shear stress at the head of pile-up may reach the level of the cohesive strength of the material, which implies a break of internal lattice barriers and smooth glide of released dislocations. Macroscopically, such effect is manifested in the form of drops of stress against strain (or time) called intermittent plastic flow (serrated yielding) [19–21]. It is worth pointing out, that this effect is characteristic of the temperatures below a threshold that is usually denoted by T_1 for low stacking fault energy materials (LSFE) and T_0 for high stacking fault energy materials (HSFE). Thus, low temperature plasticity is subdivided into two domains: temperatures above the threshold with the smooth plastic flow and temperatures below the threshold with the occurrence of the serrated yielding [3,22]. It is worth pointing out, that the threshold for stainless steels is usually close to some 30 K, which implies the serrated mode observed in liquid helium (4.2 K) and smooth plastic flow observed in liquid nitrogen (77 K). For the temperatures above the threshold, the classical models of plastic flow, including type Huber-von Mises-Hencky yield surface and mixed isotropic-kinematic hardening, can be applied. On the other hand, for the temperatures below the threshold, special models including four stages of individual serration have to be applied: elastic loading, smooth plastic flow, drop of stress and relaxation. Such models were recently developed in the literature ([3,21,22]). Another important phenomenon that affects low temperature plasticity is the phase transformation, resulting from the fact that many materials, including stainless steels, are metastable and transform from the parent

phase to the secondary phase when strained at very low temperatures. In particular, the stainless steels of family 304 transform from the austenitic (fcc) phase to the martensitic (bcc) phase, which is accompanied by local lattice distortion as a result of the volume increase, and implies occurrence of the so-called transformation induced plasticity (TRIP) [23]. Thus, the phase transformation strain should be accounted for when modelling the plastic flow ([4,11,23]). It is worth pointing out, that the phase transformation may occur both below the threshold and above the threshold temperature, which means that the inclusions of the secondary phase are observed in a wide range of temperatures (up to the temperature denoted by M_d). Description of the plastic strain induced phase transformation includes first of all the kinetics, that reflects the volume fraction of secondary phase as a function of plastic strain. Identifying the kinetics is of major importance for the constitutive model. As the phase transformation may be coupled with the intermittent plastic flow (serrated yielding) or with smooth plastic flow, the constitutive model usually depends on the temperature range. Fracture is a phenomenon of primary importance for extremely low temperatures because of the possibility of occurrence of brittle fracture, that may have catastrophic effect on the behavior of structures operating in near-0 K temperature range. Therefore, fracture shall be investigated both in intermittent plastic flow range, and in the smooth plastic flow range above the threshold temperature. In the case of stainless steels, usually ductile fracture is observed, however, it is not clear whether the macrocrack propagation is correlated with the serrated yielding and if the phase transformation may affect its evolution. Thus, the present paper essentially addresses the problem of the way the fracture occurs in thin-walled shells made of metastable materials (stainless steels) and subjected to complex loads at the temperatures not far from absolute zero.

2. Materials and methods

In order to conduct experiments at the temperatures close to absolute zero, it was necessary to use a specialized set of research equipment, dedicated to low-temperature range (see Figure 1). Completely unique apparatus uses liquefied gas as a cryogenic medium to obtain the temperature required in the test. It is transported from the helium dewar to the cryostat via the helium transfer line. It allows to obtain the laminar flow of the cooling medium, which is necessary to ensure a stable temperature during the test. Maintaining the temperature inside the cryostat is possible thanks to a thermos consisting of two tanks separated by a vacuum. The sample with the cryostat rack and sensors is placed inside the thermos. The level of helium in the cryostat is controlled by a sensor located at the top of the kit, significantly above the test sample. During the test, the helium level does not drop below the sensor level, which ensures a constant temperature around the sample. Two types of tests were performed: compound load tests and classic quasi-static uniaxial tensile tests. During uniaxial tensile tests, the sample is mounted inside the cryostat at the bottom of the cryostat between the grips (see Figure 1a). The lower handle is attached to the cryostat frame, and the upper handle is attached to the spindle. The sample during the test is equipped with a set of sensors. The force is measured with a piezoelectric force transducer. It is located inside the cryostat, right behind the sample. There are special clip-on extensometers placed on the sample, used to measure the elongation of the measuring part of the sample. The sample temperature is measured with a cryogenic thermistor located in the center of the sample measuring section. A specialized kit designed for tests of complex load is used (see Figure 1b). The sample twisting moment is obtained by means of a DC motor equipped with a worm gear. Both the force and the torsional moment with vectors parallel to the sample axis are recorded by a multi-axis force sensor at the top of the sample, calibrated for measurements at 4.2 K. The axial elongation of the sample was measured with the linear variable differential transformer (LVDT). In both tests, the cryostat was placed in a high-rigidity testing machine, and the signals from the sensors were recorded using an independent data acquisition system.

Due to the limited space inside the cryostat and the stiffness, it is necessary to use specially designed samples which, thanks to their small volume, have a small temperature gradient. The samples were made of austenitic steel 304, the composition of which is given in Table 1. For tests under complex loads, cylindrical samples were designed with a measuring length in the form of a thin-walled cylinder with a thickness that allows the test to be carried out.

Cylindrical samples were subjected to tension and torsion in accordance with loading program, which assumed that only the tensile force was applied in the first stage, and then the torsional moment was added. In order to study microstructure evolution induced by a complex stress state, two kinds of tests were performed. The first one was ended with the sample rupture (complete propagation of the macrocrack), while the other was interrupted before the initiation of the macrocrack.

As a result of the tests, samples were deformed under cryogenic conditions. In order to study the distribution of the martensitic phase volume fraction, measurements were made by magnetic induction method with the use of the feritscope (model FMP 30, Helmut Fischer

Table 1
Chemical composition of grade 304 stainless steel.

Chemical composition of 304							
C	Si	Mn	P	S	Cr	Ni	N
0.07	0.8	2.00	0.045	0.03	17–19	9–11	–
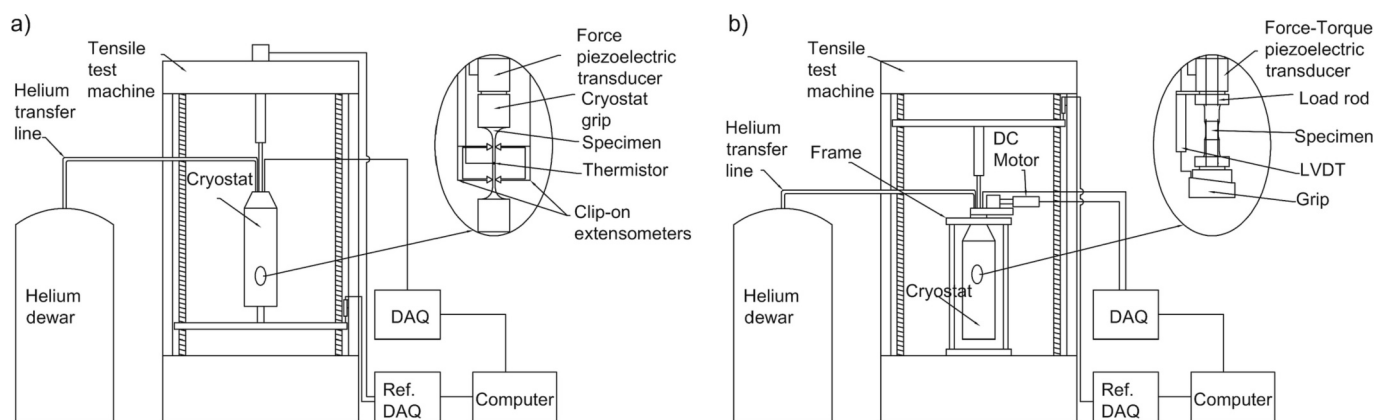
Fig. 1. Experimental set-up: (a) cryostat containing the insert with the sample and suitable instrumentation (extensometers, force transducer, thermistors, etc.) inside the traction machine, helium transfer line and the data acquisition system, (b) set-up for testing tubular samples under complex loads (traction and torsion) including suitable data acquisition system.

GmbH). During the phase transformation, the magnetic properties of the material change. Paramagnetic austenite is replaced by ferromagnetic martensite α', which makes it possible to identify the volume fraction of the phase formed as a result of deformation. In order to eliminate measurement errors induced by the curvature of the cylindrical specimen which leads to the lack of perpendicularity between the head and the studied surface, a special stand was designed (Fig. 2). The specimen is fixed in holders that enable its manual rotation about the axis as well as longitudinal displacement so as to examine a selected measurement path. It should be emphasized that the measurement result at a given point represents the averaged content of the ferromagnetic phase in the surroundings with a radius of 0.2 mm.

Measurements were performed along sixteen lines parallel to the sample axis, equally spaced apart. The distance between adjacent points on the measurement path amounts to 0.2 mm. In this way, the grid of local martensite contents was obtained. Performing interpolation, the second phase distribution was determined. In order to obtain actual contents of martensite α' (ξ), it is necessary to apply a series of corrections, which allow for the influence of the kind of the measured ferromagnetic phase (CM), sample thickness (CF_T), surface curvature (CF_C) and the distance of the measuring point from the free edge (CF_E)[25].

$$\xi = \xi_{Fr} \cdot CM \cdot CF_T \cdot CF_C \cdot CF_E \qquad (7)$$

Martensite α', which is the subject of measurements, gives lower indications in the magnetic hysteresis loop than registered ferrite δ (ξ_{Fr}). Thus, on the basis of works by Juho Talonen [26] and Glage et al. [27] the *CM* coefficient equal to 1.7 was adopted. The remaining coefficients were obtained by interpolating the values provided by the manufacturer.

The complex load applied to the thin-walled specimen leads to a loss of stability. In order to take into account the resulting structural effect, the surface topography of the non-ruptured sample was identified. Using an optical profilometer (model VR 5000, Keyence, Belgium), measurements were made of 8 areas (2.4 mm x 7 mm) surrounding every second line examined by the feritscope. A single region is characterized by a grid of points spaced every 0.024 mm, the heights of which relative to a ideal cylindrical surface are determined with an accuracy of 1 μm. The constituent areas were joined along a generatrix selected from the overlap zone in such a way that the difference in the registered heights

of the points belonging to the contact lines of adjacent regions is minimal. The profilometric measurements combined with codes written in the MATLAB environment (R2019b, MathWorks, Natick, MA, United States) allowed to accurately reconstruct the three-dimensional geometry of the sample in the gauge section.

The crystal structure, phase composition and global texture of two specimens, non-fractured and ruptured, were studied with high-energy X-ray diffraction measurements using the beamline P07B (87.1 keV, $\lambda =$ 0.0142342 nm) at DESY in Germany, Hamburg. Diffraction patterns for the phase analysis were registered in the so-called continuous mode using the area Mar345 Image Plate detector [28,29]. Experimental setup for phase analyses includes rotation by 180 degrees about the ω-axis to avoid the effect of crystallographic texture. Secondly, the obtained 2D data were converted by the Fit2D software and presented in a graph of relative intensity versus 2Theta angle. Texture measurement, for its part, was measured using a 5 × 5 counting grid with steps of $\Delta 5°$ in ω (36 images). The beam size was 0.8 × 0.8 mm^2. Pole figures were computed with the use of the software StressTexCalculator and Labotex software [30]. EBSD analysis was carried out by FEI Quanta 3D field emission gun scanning electron microscope (SEM) equipped with Trident energy-dispersive X-ray spectrometer (EDX) produced by EDAX and TSL electron backscattered diffraction (EBSD) system, as well as by Zeiss EVO 10 scanning electron microscope with Bruker backscatter detector. Samples for EBSD mapping were mechanically polished and then etched electrolytically at room temperature with an electrolyte of nitric acid (vol. 1/3) and methanol (vol. 2/3). The analysis of results was performed with the use of MTEX software (5.7.0) [31] in MATLAB environment.

The Abaqus software was used to prepare the numerical model and simulate two kinds of complex load tests, interrupted and complete one. At the beginning of model preparation, the sketch with the exact same size as the real specimen was drawn (see Fig. 2b), then 2D geometry was revolved around the symmetry axis to obtain the cylindrical shape of the sample. Discretization of the model was conducted with the use of the mapped mesh technique in the gauge area of the sample in order to increase the accuracy of the results. For the rest of the model, the mesh was generated automatically. The mapped mesh technique was introduced to ensure the desired uniform size of the elements and their proper shape (aspect ratio). It is used brick elements with reduced integration (C3D8R) which are not affected by the locking problem
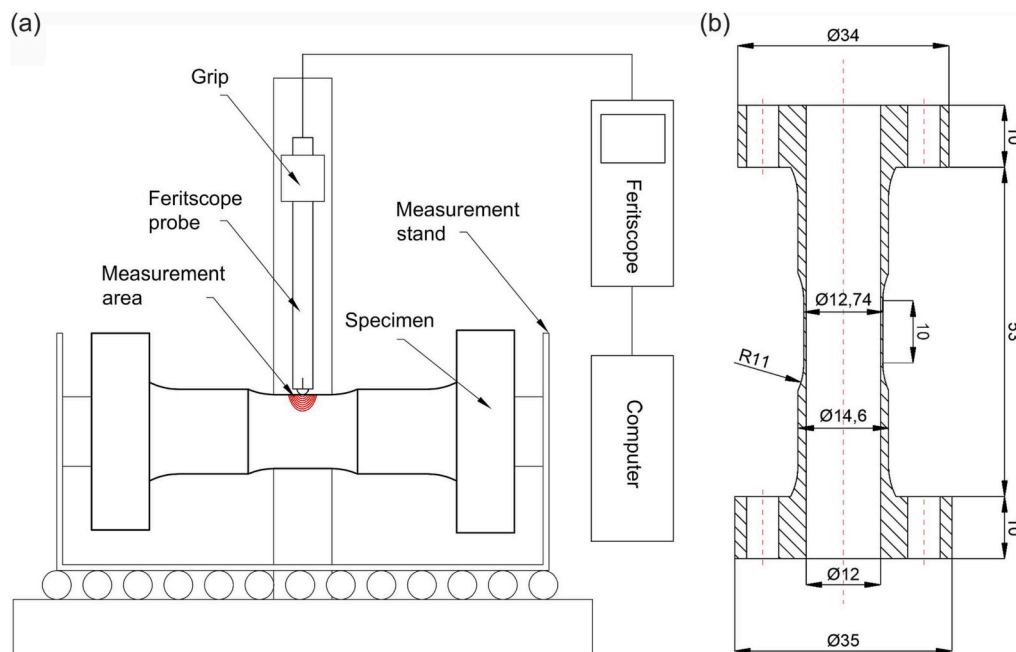

Fig. 2. (a) Stand for studying the distribution of the martensitic phase with the use of a feritscope. (b) Geometry of the cylindrical specimen, dimensions in mm.

(deformation blocking that hinders the solution convergence). Moreover, to avoid such errors, a minimum of two elements were placed on the entire sample thickness. Finally, the model consists of 16180 elements and 27413 nodes. The solution time for each of the considered cases was more than 72 h with 16 CPUs. Further refining the mesh was ineffective - it extended the computation time without improving the quality of the solution.

In order to stay close to the experiment, the appropriate program of displacements and boundary conditions were implemented. They are presented in Fig. 3. The applied boundary conditions fully correspond to the way the cylindrical sample was mounted inside the cryostat. At the bottom extremity of the model, the nodes were blocked in the longitudinal and radial direction, whereas at the top extremity the nodes were guided in such a way to impose the longitudinal and the angular motion, keeping simultaneously the straight axis of the sample.

The numerical analysis is based on the constitutive model, in which the rate independent plasticity including the isotropic hardening is applied. In the range of nearly perfect plasticity, the yield surface is assumed in its classical form, using the stress intensity σ_i

$$f(s_{ij}) = \sigma_i - \sigma_0(T) = \sqrt{\frac{3}{2} s_{ij} s_{ij}} - \sigma_0(T) \tag{8}$$

where s_{ij} is the deviatoric stress and σ_0 is the flow stress of a constant value for a given temperature T. Moreover, it is assumed that the associated flow rule holds, and the yield function constitutes potential for dissipation for the plastic strains:

$$\dot{\varepsilon}_{ij}^p = \lambda f,_{\sigma_{ij}}, \tag{9}$$

where 'dot' denotes the time derivative, and 'comma' denotes derivative with respect to the indicated variable. In the range of linear hardening (above ε_R), the elastic–plastic model with linear isotropic hardening has been implemented:

$$f(s_{ij}) = \sigma_i - \sigma_R(T) = \sqrt{\frac{3}{2} s_{ij} s_{ij}} - \sigma_0(T) - R(T) \tag{10}$$

where R denotes the isotropic hardening parameter, that obeys the following evolution law:

$$\dot{R} = C_R \dot{p}, \tag{11}$$

and p constitutes the accumulated plastic strain. In the above model, the effect of the stress–strain oscillations has been neglected since apparently it has a minor effect on the macrocrack propagation. Finally, based on the available experiments, the following parameters of the material model were identified for stainless steel 304 at 4.2 K (see Table 2):

The main purpose of the numerical analysis is to investigate the deformation and the stress fields in conjunction with phase

Table 2
Constitutive model assumed for FEM analysis.

E [GPa] elasticity modulus	σ_0 [MPa] yield stress	R [MPa] hardening modulus	ε_R hardening threshold
195.23	1269	2245	0.09

transformation evolution as well as to recreate the fracture propagation around the cylindrical specimen. To model the crack development, two FEM runs are required. Firstly, a buckling simulation is done to predict the modes of loss of stability to determine its influence on sample shape. Secondly, chosen mode shape is incorporated into the sample geometry as imperfection (with appropriate coefficient) and non-linear simulation is performed with extended finite element method (XFEM). The sample is subjected to complex loads and macro-crack is propagating around the sample. In order to simulate the fracture in an extensive way, the nonlinear deformation analysis (nlgeom), comprising large displacements and rotations as well as large strains was included.

In comparison to the conventional FEM, the eXtended Finite Element Method offers significant advantages in the modelling of macro-crack propagation. Usually, in the traditional FEM, the presence of a crack is developed by forcing the crack to adhere to certain path ex. edges of the elements. As opposed to, the crack tool, which is using XFEM to calculate the crack propagation, requires only the area (chosen by user) in which it may occur and spread, which provides versatility in modelling. The method is based on the enrichment of the FE model with additional degrees of freedom (DOFs) that are tied to the nodes of the elements crossed by the propagated crack. In this approach, the discontinuity is included in the numerical model without modifying the discretization, because the mesh is generated without considering the existence of the crack. In addition, the nodes nearby the crack tip are enriched with additional DOFs associated with functions that replicate the asymptotic LEFM fields. This allows the modelling of the crack incoherence within the crack-tip element and considerably improves the accuracy in the computation of the stress intensity factors (SIFs).

Damage initiation refers to the beginning of degradation of the cohesive response at a contact point. The process of degradation begins when the contact stress and/or contact separation satisfy certain damage initiation criteria. Each initiation criterion has an output variable associated with it, to indicate whether the criterion is met. A value of one or higher denotes that the initiation criterion has been met. Several fracture criteria are available, mainly divided in two groups: stress and strain based. In Table 3 four fracture criteria available in Abaqus software are presented.

In presented work the maximum principal strain criterion is used. In this criterion ε_{max}^0 signifies the maximum permissible principal strain. Similar approach was not described in the literature, due to the lack of crack propagation simulations at the 4.2 K temperature. Therefore, a criterion often used for cracks in objects of similar shape to the analyzed sample was adopted. Das et al. [33] applied a threshold for equivalent plastic strain in the failing area to examine fatigue fracture. Adeeb and Horsley [34] employed 20 % maximum principal strain as the critical strain for safe excavation of defective pipes, considering that material fails at 20 % strain. For cryogenic temperatures the authors in [35,36] are using the Modified Mohr–Coulomb (MMC) phenomenological
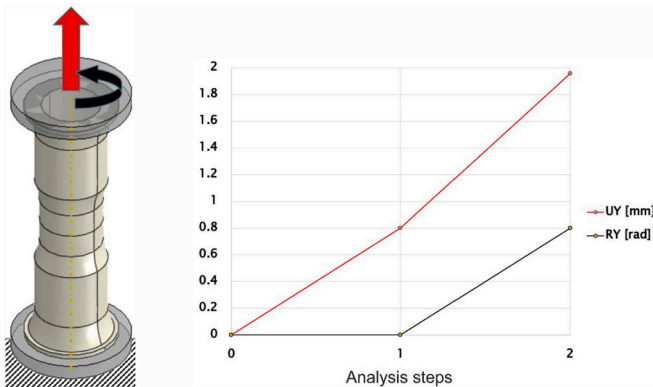
Fig. 3. Numerical model of the cylindrical shell: boundary conditions and the program of displacements comprising combination of elongation and rotation.

Table 3
Fracture criteria [[32]].

Maximum principal stress criterion:	$s = \left\{ \frac{<\sigma_{max}>}{\sigma_{max}^0} \right\}$
Maximum principal strain criterion:	$s = \left\{ \frac{<\varepsilon_{max}>}{\varepsilon_{max}^0} \right\}$
Maximum nominal stress criterion:	$s = max\left\{ \frac{<t_n>}{t_n^0}, \frac{t_s}{t_s^0}, \frac{t_t}{t_t^0} \right\}$
Maximum nominal strain criterion	$s = max\left\{ \frac{<\varepsilon_n>}{\varepsilon_n^0}, \frac{\varepsilon_s}{\varepsilon_s^0}, \frac{\varepsilon_t}{\varepsilon_t^0} \right\}$

fracture criterion. Their fracture model depends on the loading history of the critical material point (the local plastic deformation is severe and its occurrence may induce failure in the material – regarding the Lode angle (O) parameter and the stress triaxiality (n).

3. Phase transformation kinetics

The phase transformation kinetics has been determined by means of suitable experiments performed on the samples extracted from the cylindrical specimens presented in (Fig. 2). Two campaigns of tests were performed in liquid helium in order to obtain the reliable results. Following the concept by Olson and Cohen, the kinetics of the $\gamma - \alpha'$ phase transformation is mostly based on the plastic strains [23]. The plastic strain induced phase transformation observed in the metastable materials (stainless steels) at extremely low temperatures is usually distinguished from the stress assisted phase transformation, characteristic of the shape memory alloys. The phase transformation occurs below the threshold temperature M_d and can be activated both in liquid nitrogen (77 K) and in liquid helium (4.2 K). In the latter case it is usually accompanied by the intermittent plastic flow (serrated yielding). The phase transformation kinetics developed by Olson and Cohen is based on the mechanism of secondary phase nucleation at the shear bands intersections and contains two temperature dependent parameters (α, β), as well as a fixed component *n*:

$$\xi = 1 - \exp[-\beta(1 - \exp(-\alpha\varepsilon^p))^n] \tag{12}$$

Such a formulation is characteristic of a wide range of temperatures, whereas, at extremely low temperatures the mathematical representation of the phase transformation can be linearized [24]. Moreover, the phase transformation occurs in the domain of small or moderately large strains. In the case of liquid helium, some limited temperature driven spontaneous phase transformation, triggered by the existing potential nucleation sites, might occur. It takes place below the temperature M_s, characteristic of a given material. Moreover, certain amount of secondary phase may preexist as a result of the technological processes engaged when producing the samples. Thus, the volume fraction of secondary phase comprises the preexisting fraction (ξ_0) due to the spontaneous phase transformation and the technological processes, and the main fraction due to the plastic strains ($\Delta\xi$):

$$\xi = \xi_0 + \Delta\xi \tag{13}$$

In view of fast phase transformation process at extremely low temperatures (liquid helium), a linearized evolution law for the volume fraction of secondary phase (martensite) has been developed:

$$\dot{\xi} = A(T, \sigma_{ij})\dot{\varepsilon}_i^p \quad ; \quad \dot{\varepsilon}_i^p = \sqrt{\frac{2}{3}\dot{e}_{ij}^p\dot{e}_{ij}^p} \tag{14}$$

where σ_{ij} denotes the stress tensor, A is function of temperature and stress, and ε_i^p denotes the plastic strain intensity. For the isothermal processes and small variation of stress, one obtains:

$$d\xi = Ad\varepsilon_i^p \tag{15}$$

where A represents constant slope of the volume fraction of martensite as a function of plastic strain at a given temperature. Given the initial amount of secondary phase, one obtains:

$$\xi = \xi_0 + A\int_0^{\tilde{t}}\sqrt{\frac{2}{3}\dot{e}_{ij}^p\dot{e}_{ij}^p}\,dt \tag{16}$$

The grade 304 stainless steel used during the tests is characterized by substantial variations of the individual alloy components. They may have direct impact on the phase transformation rate. The chemical composition of tested austenitic stainless steel is shown in Table 1. The samples subjected to uniaxial tension in liquid helium were extracted directly from the same samples that were used for the complex loads

testing. Thus, the same chemical composition was assured. During the tests, the samples were stretched to a predetermined force and unloaded. After each step the sample was removed from the cryostat and, as soon as the temperature reached ambient value, the measurements were carried out. The examination by means of the feritscope was carried out every 0.2 mm along the gauge length of the sample. The phase transformation profiles, measured along the generators of the cylindrical sample, are for comparison illustrated in (Fig. 4a). Additional measurements by means of the feritscope were carried out on the uniaxial specimens extracted from the cylindrical sample and tested in liquid helium. Finally, by combining the average martensite content with the sample elongation, a diagram corresponding to both test campaigns (I, II) was obtained (Fig. 4b). Given the postulated linearization of the transformation curve, the increment of the volume fraction of new phase (martensite) is directly proportional to the increment of the plastic strain intensity under the isothermal conditions ($T = const$). Eventually, the following parameters of the phase transformation kinetics were identified for grade 304 stainless steel under consideration:

$$\xi_0 = 0.8 \quad ; \quad A = 2.92 \tag{17}$$

Thus, based on the uniaxial tests, the linear representation of the phase transformation kinetics for grade 304 stainless steel at 4.2 K reads:

$$\xi = \xi_0 + A\varepsilon_i^p \tag{18}$$

Using the above formula, the martensite content was calculated on the basis of the plastic strain intensity in FEM post processing.

4. Structural stability and microstructure evolution before the onset of fracture

The phase transformation study under the influence of complex loads is carried out in two stages. The first involves identification of the martensite α' distribution and determination of the primary and secondary phase texture along with EBSD imaging, before fracture initiation. A detailed plan of the applied displacement and rotation as well as the resulting stress–time dependencies are presented in Fig. 5. After exceeding the nominal tensile stresses $\sigma_N = 967$ MPa and the maximum shear stresses due to torsion $\tau_{Nmax} = 253$ MPa, discontinuous plastic flow begins, which is stopped at the relative elongation of the gauge length $\varepsilon_N = 0.2$ and the torsion angle $\Delta\varphi = 35.5°$. The achieved deformations and the associated nominal stresses $\sigma_N = 824$ MPa, $\tau_{Nmax} = 388$ MPa are maintained, and then the specimen is gradually unloaded.

Initially, the cylindrical shell is in a membrane state. The system of stresses constitutes a superposition of those originating from tension and torsion. In the elasto-plastic range, torsion leads to a bifurcation loss of stability. The tensile share reduces the amplitude of the circumferential waves. The significant advantage of tensile stresses in relation to shear stresses due to torsion can even completely eliminate the buckling effect. The examinations conducted with the use of an optical profilometer revealed that the implemented complex load path causes a loss of stability and the thin walled cylinder takes the buckling form n = 3. Thus, the phase transformation is controlled by three factors: tension, torsion, and local bending related to buckling. The distribution of martensite α' volume fraction in the gauge section was identified by a magnetometric method using a feritscope (Fig. 6).

The secondary phase is concentrated in the band areas with the direction of the buckling folds. The distribution of the martensite shows a distinct asymmetry. The phase transformation is more intensive in the upper part of the gauge zone, as it is activated by the movement of the upper specimen head: rotation towards positive *x* values and displacement along the *y* axis. The lower specimen head remains fixed. In addition to the examination of the sample surface by means of a feritscope, the measurement was performed using a non-contact profilometer. In this way, the geometry of the buckled specimen was identified with an accuracy of 1 μm. Combining the results obtained

(a)

(b)
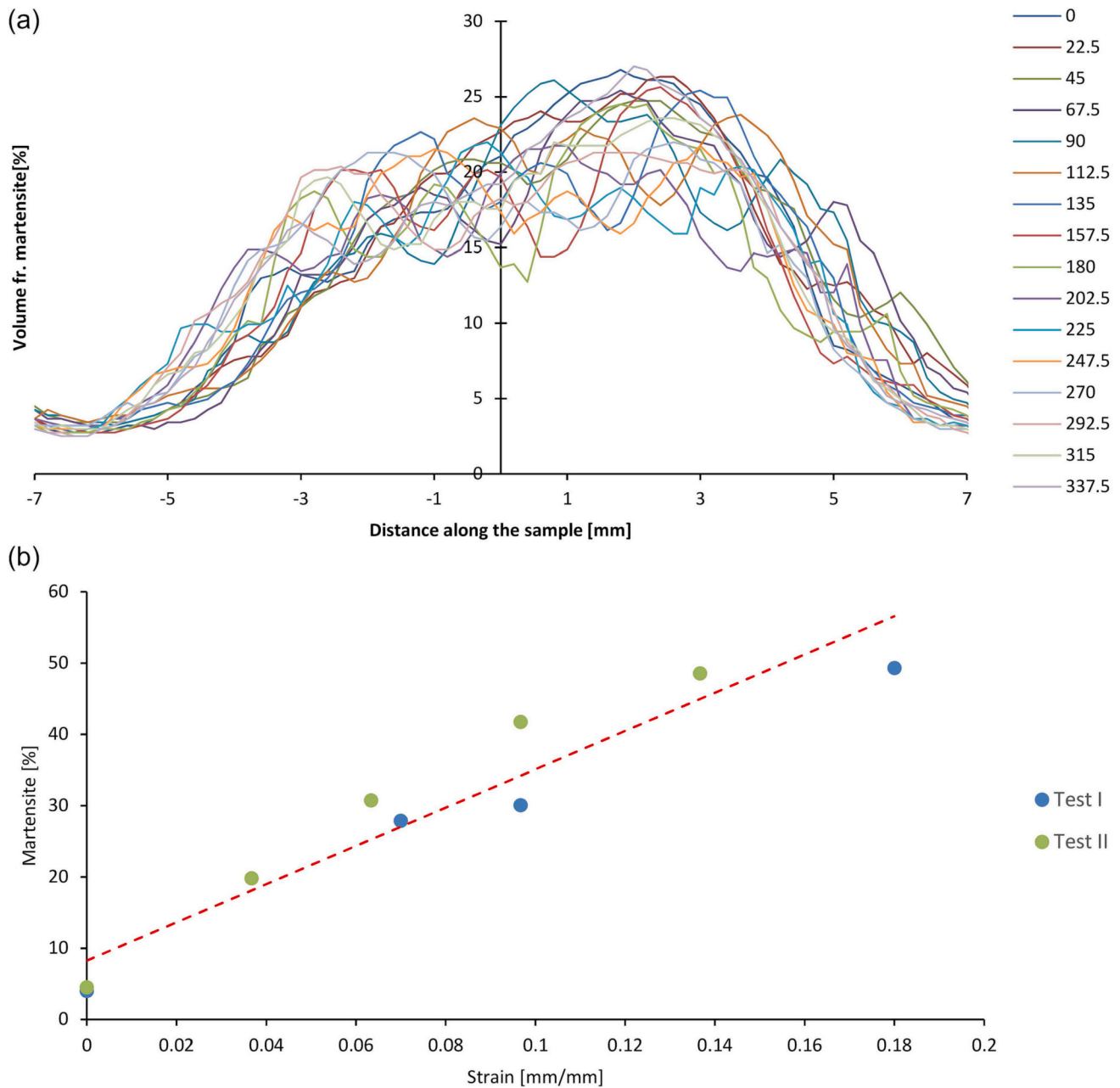
Fig. 4. (a) Distribution of secondary phase along the generators of the cylindrical sample (every 22.5 deg), (b) experimentally determined phase transformation kinetics for grade 304 stainless steel at 4.2 K.

with two different experimental techniques allowed to detect the coupling between the deformation of the thin-walled cylinder and the distribution of the secondary phase (see Fig. 7a). Martensite clearly prefers the slopes of the buckling folds, continuing its growth towards the well centers, while it is unwillingly formed on the fold ridges. This observation allows us to draw a conclusion about the key role of shear stresses in the activation of the phase transformation. The maximum shear stresses reach the greatest values in the slopes of the bending forms of the loss of stability. The distribution of the key maximum shear stresses is approximated by the FEM simulation (Fig. 7b). In the numerical model, a single buckling fold is composed of two parts taking the forms of wedges. The areas of the highest shear stresses arise on their sharp slopes (1, 1'), while on the remaining ones with a lower decrease, the shear stresses take smaller but significant values (2, 2'). In the central part of the sample, the maximum shear stresses are reduced due to the dominance of tensile stresses induced by the necking. The

characteristic pattern of the highest shear stresses is not exactly repeated in the experiment. Instead of a localized necking visible in the numerical model, the sample cross-section is uniformly reduced along the gauge length. Thus, the depressions due to the loss of stability begin to play an important role. Inside them, the dominance of tensile stresses is eliminated by compressive stresses, which leads to an increase in maximal shear stresses. Thus, the martensite initiated on the fold slope, in the area of the highest shear stresses (1 in Fig. 7a), develops towards the well center. The form of loss of stability identified experimentally differs from the ideal one predicted by FEM. Incompletely formed folds with lower amplitude arise mainly in the lower part and vanish in the upper part. As a result, the martensitic transformation begins at the ends of the elevations in the upper part of the sample, where stronger topographic gradients occur (points 3,4,5).

It turns out that in the areas of maximum shear stresses predicted by the FEM method, there is an almost plane state of stress, similar to that
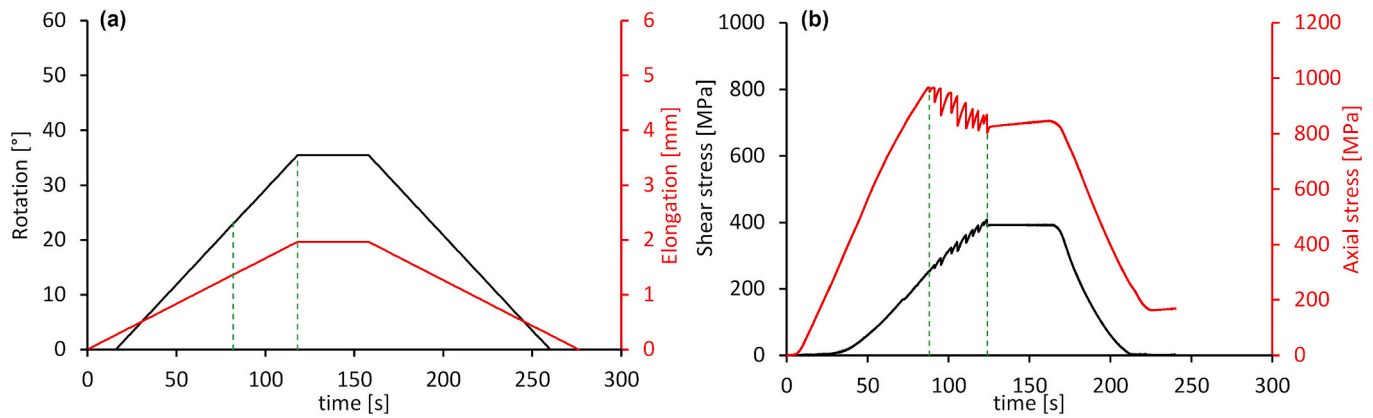
Fig. 5. (a) Load program assumed for the first stage of investigations (b) nominal tensile (σ_N) and shear stresses (τ_N) versus time.
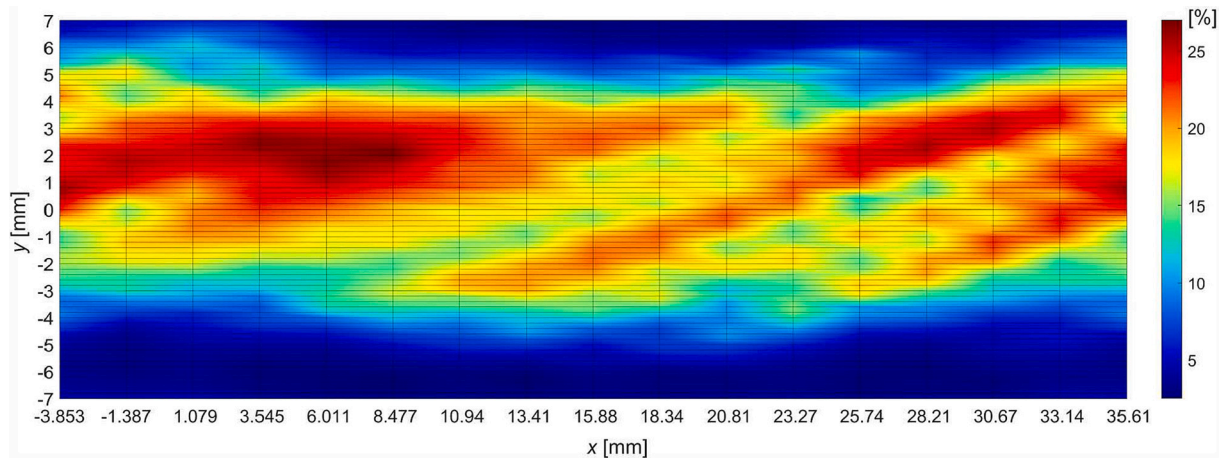

Fig. 6. Martensite α' volume fraction in the unfolded surface of the cylindrical specimen subjected to the first stage of the complex load path. The axis y is parallel to the specimen axis and $y = 0$ is at the gauge length center.
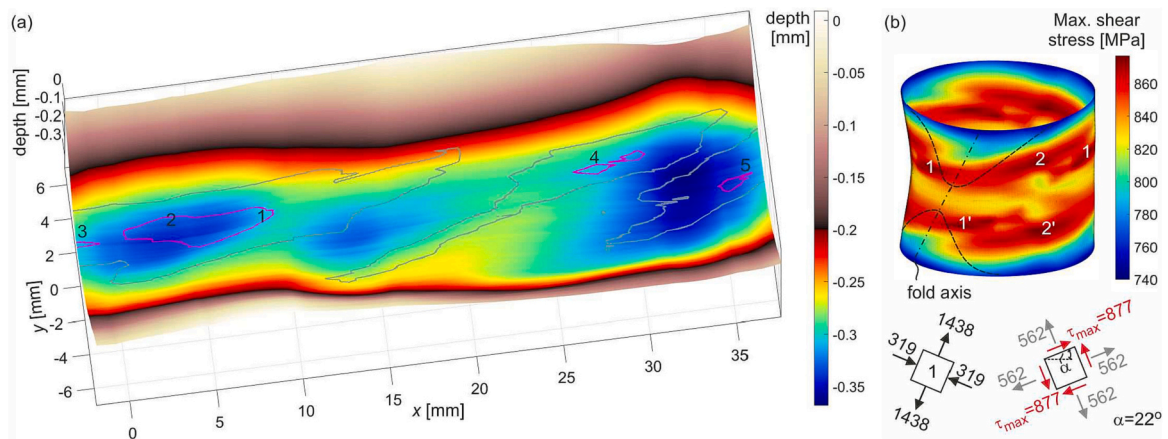

Fig. 7. (a) Topography of the unfolded surface of the cylindrical specimen subjected to the first stage of the complex load path. The graph is combined with contours of the martensite volume fraction map at 20% (gray) and 25% (magenta). (b) FEM reconstruction of maximum shear stresses distribution superimposed on the deformed specimen. In the points with the highest values (1, 1'), the state of stresses in the principal axes is presented and the maximum shear stresses are visualized. The buckling fold is marked with dashed lines.

generated by tension combined with torsion. The influence of bending due to buckling is small. It can be seen that the principal stress system resulting from simultaneous action of the torsional moment and the stretching force determines the buckled shape of the cylinder. The vector of maximum tensile stress is parallel to the longitudinal direction of the

buckling fold, and the vector of minimum compressive stress remains perpendicular to it (Fig. 7b). This particular stress state leads to arising, in the cylinder surface, a system of the highest shear stresses rotated by 22° in relation to the transversal direction of the specimen (TD).

The FEM method enabled to accurately characterize the regions of

the specimen with the highest content of martensite generated in the places of the highest shear stresses. The question arises as to how the detected intensified phase transformation proceeds. For the purpose of in-depth analysis, EBSD investigations were performed. A series of images of the region 1 (Fig. 7a) were taken, where the feritscope measurements identified the maximum 27% martensite content.

EBSD studies show that the primary phase clearly prefers the Goss and Cu orientations. These components form the dominating texture fiber $\tau \langle 1\,\overline{1}\,0 \rangle_\gamma \parallel$ TD. The analysis of the orientation distribution function (ODF) (Fig. 8a) shows that the volume content of the fiber τ in the orientation space amounts to 38%. The reason for such a high preference is the specific position of the close-packed direction $\langle 1\,\overline{1}\,0 \rangle_\gamma$. In the grains belonging to the fiber τ, it is oriented along the TD perpendicular to the direction of the tensile force and the torsional moment vector. It is worth noting that the position does not change after the loads are applied. Torsion is particularly important as, inducing shear deformation, it retains the directions of material fibers parallel to TD and introduces rotation of those along LD. The direction of close packing $\langle 1\,\overline{1}\,0 \rangle_\gamma$ plays a key role in the phase transformation. It remains invariant, does not rotate and change length, during the Pitsch and the Kurdjumov–Sachs paths most often found in austenitic steels loaded in cryogenic conditions. Thus, in the grains belonging to the fiber τ, one of the most important transformation conditions is preserved. The detailed characterization of the secondary phase embedding in the austenite is presented in a representative EBSD image (Fig. 8). In a grain with the Goss orientation, band-like martensite α' is formed just along the direction TD. It continues in the adjacent grain with the orientation Cu. This time, however, the transformation is more intense. Martensite α' arises not only in planes $(\overline{1}\,1\,1)_\gamma$ perpendicular to the LD, but also in $(\overline{1}\,\overline{1}\,1)_\gamma$ obliquely oriented. The initially cross-shaped martensite grows retaining a lamellar shape. The oblique bands of the secondary phase are generated in the shear system $[\overline{2}\,1\,\overline{1}](\overline{1}\,\overline{1}\,1)_\gamma$ with a high Schmid factor

(0.43) determined for the prevailing complex stress state. The main source of significant resolved shear stresses that induce the phase transformation is τ_{max} discussed earlier. It is worth noting that the martensite bands with a direction close to TD are activated in a system $[1\,2\,1](\overline{1}\,1\,\overline{1})_\gamma$ with much lower Schmid factor (0.34). The willingness to form this type of plates results from invariance of the direction $[110]_\gamma \parallel$ TD during torsion.

The mechanism of martensite cross-growth was especially clearly recorded in the Cu grain, which underwent almost complete phase transformation (Fig. 9). The orientation of the austenitic matrix causes the transformation to be activated in two systems with the highest resolved shear stresses $[2\,\overline{1}\,1](1\,1\,1)_\gamma$ and $[1\,1\,2](\overline{1}\,1\,\overline{1})_\gamma$. The first grain of martensite α' is generated in the plane $(1\,1\,1)_\gamma \parallel (1\,0\,1)_{\alpha'} \perp$ LD retaining the invariance of the direction $[\overline{1}\,0\,1]_\gamma \parallel [1\,\overline{1}\,\overline{1}]_{\alpha'}$ TD. Thus, when embedding in the austenite, it takes the Kurdjumov–Sachs disorientation. It turns out that the twin of the formed grain has the ability to develop along the second, activated austenite plane. The twin relation is formed by rotation around the axis $\rho = [1\,\overline{1}\,1]_{\alpha'}$ by the angle $\omega = 60°$. Thus, the orientation of the second martensite grain can be expressed by the coordinate transformation matrix as follows:

$$L_{M2} = L_{M1}T, \tag{19}$$

where L_{M1} and T are the coordinate transformation matrices of the first martensite grain and the martensite twin:

$$L_{M1} = \begin{bmatrix} -1/\sqrt{2} & 0 & -1\sqrt{2} \\ 1/\sqrt{3} & -1/\sqrt{3} & -1\sqrt{3} \\ -1/\sqrt{6} & -2/\sqrt{6} & 1\sqrt{6} \end{bmatrix}, \quad T = \frac{1}{3}\begin{bmatrix} 2 & -2 & -1 \\ 1 & 2 & -2 \\ 2 & 1 & 2 \end{bmatrix} \tag{20}$$

thus:
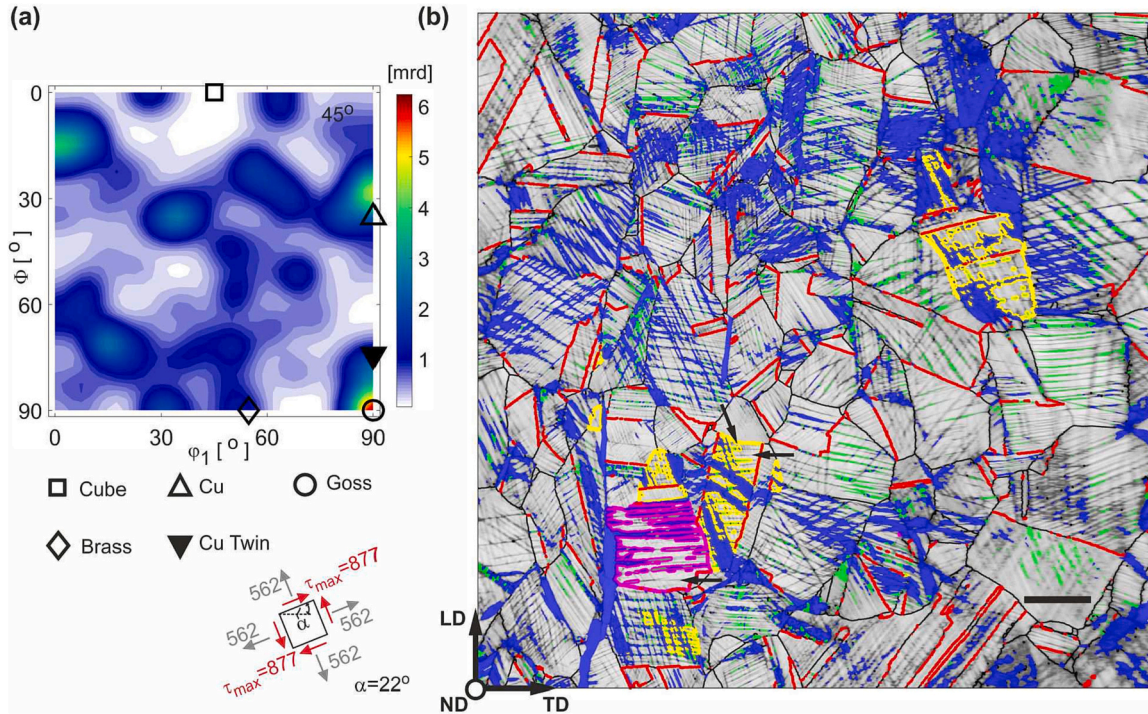
Fig. 8. Microstructure of the region with the highest shear stresses. (a) Section $\varphi_2 = 45°$ of the austenite ODF in the Euler space. (b) Image quality map of austenite with martensite α' (blue) and martensite ε (green). Austenite boundaries are marked with black lines, and those that meet a twin relationship are marked in red. The grains with Goss and Cu orientation are distinguished in magenta and yellow, respectively. The shear bands activated in them are indicated by arrows. Scale bar: 10 μm.
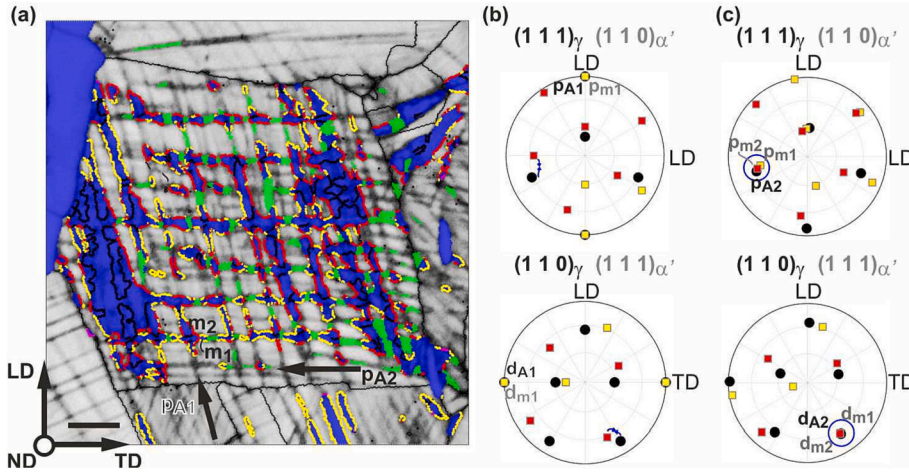
Fig. 9. (a) Image quality map of the austenite grain which undergoes a transformation into martensite with cross morphology. The arising martensite α' and ε are denoted in blue and green, respectively. Interphase boundaries with disorientation Pitsch and Kurdjumov–Sachs are distinguished in red and yellow. The traces of active shear planes $\mathbf{p}_{A1}$ and $\mathbf{p}_{A2}$ are indicated by arrows. Scale bar: 2 μm. (b) Pole figures of close-packed planes and directions of the Cu-oriented austenite grain (black dots). For comparison, the position of close-packed planes and directions belonging to the martensite grain with disorientation Kurdjumov–Sachs (yellow triangles) and its twin (red triangle) is marked. (c) Pole figures of close-packed planes and directions of the registered austenite grain (black dots) compared to analogical ones belonging to the crossed martensite grains m_1 (yellow triangles) and m_2 (red triangles).

$$\mathbf{L}_{M2} = \frac{1}{3}\begin{bmatrix} -4/\sqrt{2} & 1\sqrt{2} & -1\sqrt{2} \\ -1/\sqrt{3} & -5/\sqrt{3} & -1\sqrt{3} \\ -2/\sqrt{6} & -1/\sqrt{6} & 7\sqrt{6} \end{bmatrix} \quad (21)$$

Using the coordinate transformation matrix of the austenitic matrix $\mathbf{L}_A$, it can be shown that the martensite twin formed does not have an exactly correlated direction and the plane of close packing, $\mathbf{d}_{M2} = [1\,\bar{1}\,1]_{\alpha'}$ and $\mathbf{p}_{M2} = [0\,\bar{1}\,\bar{1}]_{\alpha'}$, with the analogous ones in austenite, $\mathbf{d}_{A2} = [0\,1\,1]_\gamma$ and $\mathbf{p}_{A2} = [\bar{1}\,\bar{1}\,1]_\gamma$,

$$\angle(\mathbf{d}_{M2}, \mathbf{d}_{A2}) = \angle(\mathbf{L}_{M2}\mathbf{d}_{M2}, \mathbf{L}_A\mathbf{d}_{A2}) = 14°, \quad (22)$$

$$\angle(\mathbf{p}_{M2}, \mathbf{p}_{A2}) = \angle(\mathbf{L}_{M2}\mathbf{p}_{M2}, \mathbf{L}_A\mathbf{p}_{A2}) = 20°, \quad (23)$$

where $\quad \mathbf{L}_A = \begin{bmatrix} -1/\sqrt{3} & -1\sqrt{3} & -1\sqrt{3} \\ -1/\sqrt{2} & -5/\sqrt{3} & -1\sqrt{2} \\ -1/\sqrt{6} & 2/\sqrt{6} & -1\sqrt{6} \end{bmatrix}. \quad (24)$

EBSD analysis shows that the necessary fitting is obtained by the rotation of the austenitic grain and embedded martensitic grains (Fig. 9b and c). Finally, the martensitic twin forms the Pitsch disorientation with austenite matrix.

The performed analysis shows that the bcc phase forms non-random boundaries with the austenitic matrix. According to the misorientation distribution function (MDF) the Pitsch disorientation dominates, accompanied by the Kurdjumov-Sach disorientation occurring at a lower frequency (Fig. 10a). The former is preferred in Cu-oriented grains,
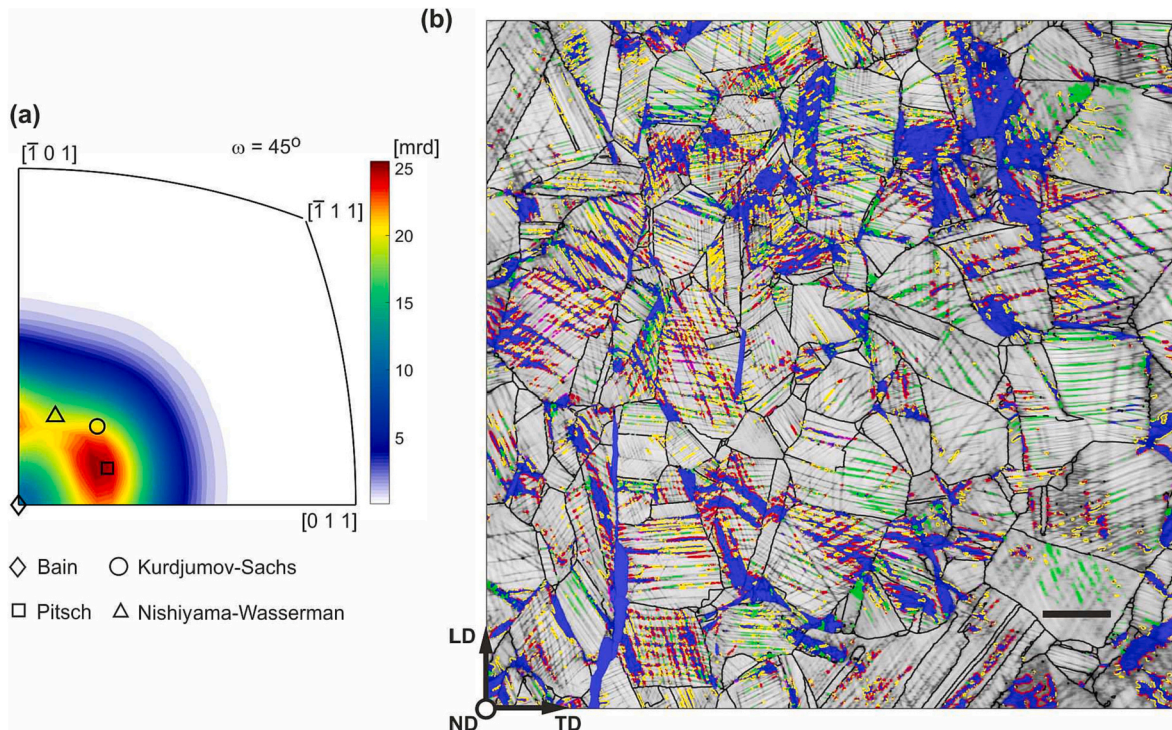
Fig. 10. Misorientation at the austenite/ martensite α' boundaries in the region with the highest shear stresses. (a) Section $\omega = 45°$ of the austenite/ martensite α' MDF in the fundamental region of the axis/ angle space. (b) Image quality map of austenite with martensite α' (blue) and martensite ε (green). Austenite boundaries are marked with black lines, while austenite/ martensite α' ones with high preferred disorientations Pitsch, Kurdjumov–Sachs and Nishiyama–Wassermann are distinguished in red, yellow and magenta, respectively. Scale bar: 10 μm.

while the latter in Goss-oriented grains (Fig. 10b). The Kurdjumov–Sachs disorientation is formed from the Pitsch one by rotation by a small angle of 5.26° about the dense packing direction of the austenite [1 0 1].

Parallel to the EBSD analysis revealing the details of the martensite growth in the austenitic matrix under the influence of complex loads, XRD investigations with the use of synchrotron beam were carried out to better understand the evolution of the microstructure. The examination performed at the point of the fold's slope, where the plane stress state prevails, shows that the martensite $\alpha^{'}$ grain with two planes $(1\,\bar{1}\,0)_{\alpha'}$ and $(1\,1\,0)_{\alpha'}$ perpendicular to the axes LD and TD (p_{m1}, p_{m2} in Fig. 11) is formed most often (1.8 mrd). Such an orientation indicates the key role of the torsional moment which, by generating shear in these planes, induces the phase transformation. This is confirmed by the appropriate orientation of the austenite. The most common grain has planes $(\bar{1}\,1\,1)_{\gamma}$ and $(1\,1\,1)_{\gamma}$ (p_{a1}, p_{a2} in Fig. 11) as well as directions belonging to them $[\bar{1}\,\bar{1}\,0]_{\gamma}$ and $[\bar{1}\,0\,1]_{\gamma}$ (d_{a1}, d_{a2} in Fig. 11) with a similar position to the martensitic ones $(1\,\bar{1}\,0)_{\alpha'}$, $(1\,1\,0)_{\alpha'}$ and $[\bar{1}\,\bar{1}\,1]_{\alpha'}$, $[\bar{1}\,1\,1]_{\alpha'}$ (d_{m1}, d_{m2} in Fig. 11). This system enables the phase transformation leading to the Kurdjumov–Sachs disorentation. The martensite $\alpha^{'}$ grain growth is not uniform. Planes perpendicular to the sample axis are more frequent than those perpendicular to LD. The reason for the observed preference is the special position of the invariant direction required during the Kurdjumov–Sachs and Pitsch transformations. The first system of planes $(1\,\bar{1}\,0)_{\alpha'}$ includes directions $[\bar{1}\,\bar{1}\,1]_{\alpha'}$ oriented close to TD. As a result, they are slightly deformed when twisted, in contrast to the directions contained in the other system.

The registered highly preferred orientation of martensite is accompanied by two other frequently occurring ones (1.5 mrd and 1.2 mrd). The latter show twin relationships with the former (see Fig. 11). Twins of the highly preferred martensite grain are obtained by rotating 60° around axes $[\bar{1}\,1\,1]_{\alpha'}$ and $[\bar{1}\,1\,1]_{\alpha'}$. The first is formed more often because it develops by shearing on planes $(1\,\bar{1}\,0)_{\alpha'}\perp$LD. The second, less common, requires shearing along the plane $(1\,1\,0)_{\alpha'}\perp$TD. The obtained results confirm the twinning-based mechanism of the martensite cross-growth.
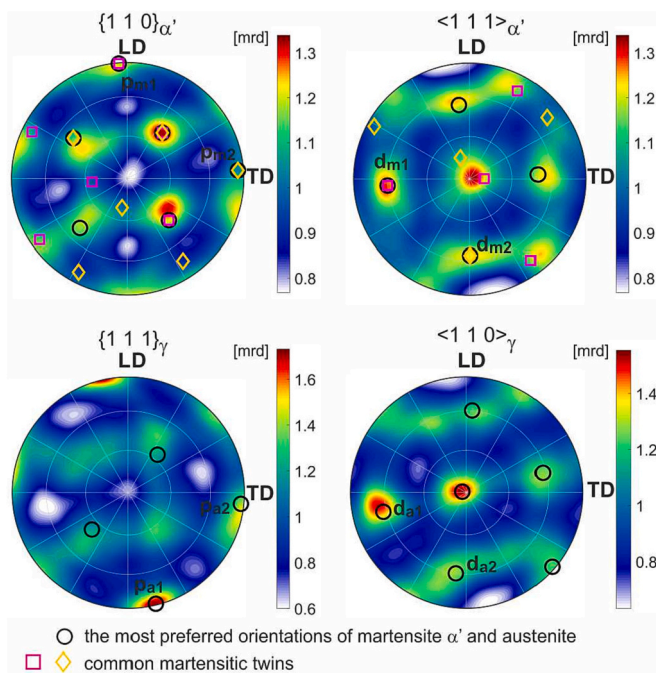

Fig. 11. PDF for close-packed planes and directions of martensite $\alpha^{'}$ and austenite.

5. Macrocrack propagation in tubular samples under complex loads

The second stage of the research includes the study of advanced phase transformation induced by complex loads as well as the analysis of coupling the generated martensite fields with the initiation and propagation of the macrocrack. The program of elongation and rotation along with the registered relationships of the nominal tensile stress and the maximal shear stress due to torsion versus time is shown in Fig. 12. At the stress $\sigma_N = 820$ MPa, the range of discontinuous plastic flow begins, followed by the material strengthening. The test ends with a macrocrack propagation (Fig. 13), after reaching $\sigma_N = 1051$ MPa and $\tau_{Nmax} = 600$ MPa.

An interesting feature of fracture trajectory in the thin-walled cylindrical specimens subjected to traction and torsion consists in the fact, that the macrocrack develops in the circumferential direction, both clockwise and counterclockwise. Thus, already at the beginning of fracture a bifurcation occurs, and two crack tips are essentially formed at point O (Fig. 14a). They move in opposite directions. One branch of the crack propagates downward according to the rotation of the specimen head. Thus, it develops much faster, circulating the sample along the helical line. The second branch, while propagating upwards, is gradually suppressed. The studies by means of the feritscope show that a very intense phase transformation occurs in this area, the martensite $\alpha^{'}$ volume fraction reaches 80% (Fig. 14a). Thus, closure of the macrocrack is associated with the secondary phase formation. On the one hand, the transformation takes over some of the fracture energy, on the other hand it produces a new, compact microstructure that blocks further fracture development. The obtained results reveal that the formation of martensite has positive effect on the mechanical properties. A similar conclusion was obtained by Z. Mei and J.W. Morris [37] by comparing fatigue crack propagation in 304L and 304LN steels. The conducted research has shown that the martensitic transformation lowers the fracture growth rate and increases the stress intensity threshold for fracture development. The observed beneficial effect results from the generated compression, which disturbs the stress field around the fracture tip, as well as from deflecting and complicating the fracture path due to the necessity to avoid embedded harder martensite plates. Thus, the weaker phase is austenite. This is confirmed by numerous studies carried out on 304L and 316L steels, which reveal a ductile cleavage induced by loading at liquid helium and liquid nitrogen temperatures [38–40].

At the specimen rupture, the propagating macrocrack reaches the upper one to separate a strip of material (comp. Figs. 13 and 14). The direct reason is the presence of the buckling folds. The fracture developing along the helical line meets an elevation, which leads to a change of direction. The macrocrack cuts the area of lower stiffness, along the cylinder generatrix and then joins the previously formed upper fragment of the macrocrack.

An additional factor determining the macrocrack trajectory is martensite $\alpha^{'}$. It constitutes secondary, harder phase and concentrating in the slopes of the buckling folds, it stiffens them. The fracture initiates at the top of the gauge section before an elevation, making it difficult to propagate according to the rotation of the sample head. The reason is not only the encountered fold, but also harder martensite $\alpha^{'}$ embedded in its slope with a compact microstructure. As a result, the macrocrack propagation in the opposite direction is promoted. Similarly, martensite $\alpha^{'}$ embedded in the slope of the second, more clearly formed fold contributes to deflecting the path of the lower part of the macrocrack, which leads to its connection with the upper branch.

The phase transformation induced by tension combined with torsion is very intense. The investigations by means of the feritscope show that the martensite $\alpha^{'}$ content in the gauge area exceeds 40%. Distribution of the secondary phase in the unfolded surface of the fractured specimen is shown in Fig. 14. High localization of the secondary phase is observed in
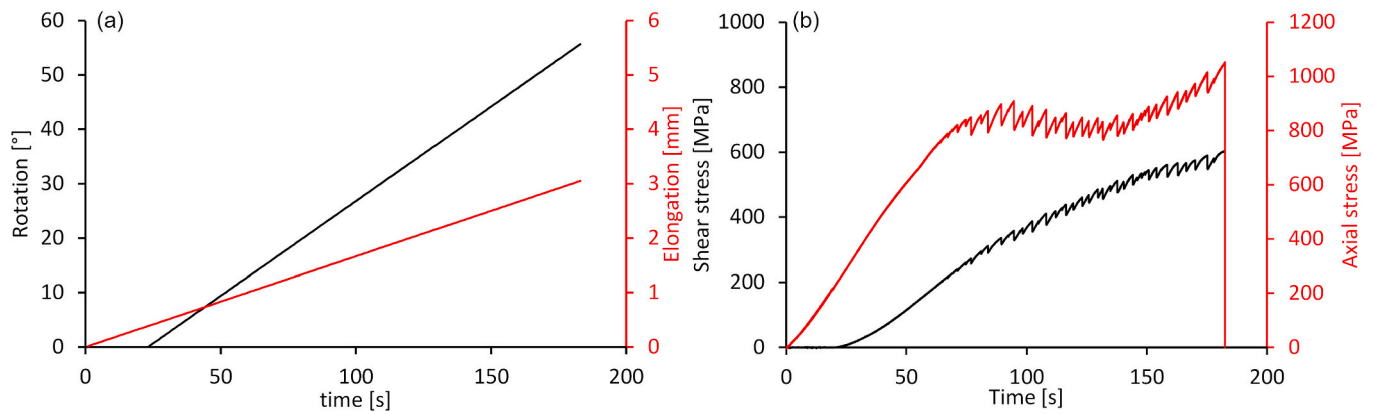
Fig. 12. (a) Loading program assumed for the second stage of investigations (b) nominal tensile (σ_N) and shear stresses (τ_N) versus time.
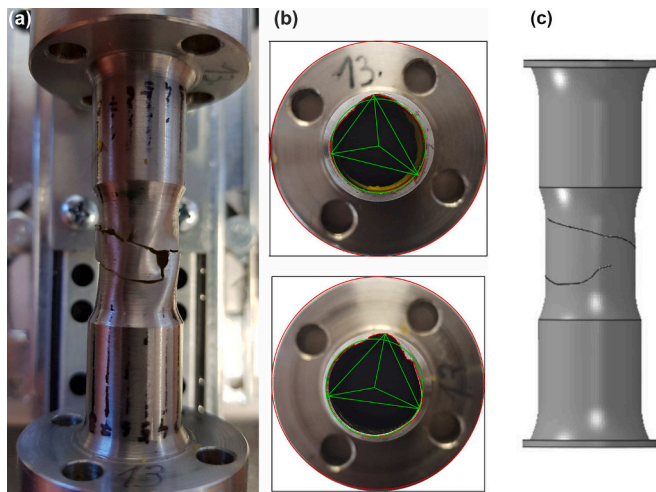

Fig. 13. (a) Circumferential fracture of stainless steel thin-walled cylinder loaded at cryogenic temperatures, (b) specimen fractured due to the complex load and distortion of the cross-section - geometrical imperfection, (c) macrocrack trajectory.

9 points along the upper part of the macrocrack was investigated by the X-ray diffraction method with the use of synchrotron radiation (Fig. 14b). The obtained results show higher content of martensite compared to that registered by the feritscope. The reason for the discrepancies is the lower accuracy of the feritoscopic measurement, which is additionally disturbed by the presence of cracks and surface curvatures. The highest volume fraction of martensite α', 83% and 82%, is identified at points 6 and 7 located on the slope of the buckling fold. The obtained result confirms that the maxima of the secondary phase content are directly related to the areas of maximum shear stresses.

6. Microstructure evolution after the onset of fracture

Continuation of the complex load path causes formation of further martensite nuclei according to the scheme described in Section 4 as well as growth of already transformed areas (Fig. 15 a). The specific microstructure clearly indicates that the phase transformation mechanism is used, based on two shear systems which, activated by the largest resolved shear stresses, form a coherent arrangement of martensite grains joined by twin boundaries. XRD studies with the application of a synchrotron beam, performed at points 4 and 9 along the macrocrack, show that in the advanced stage of transformation, the most often formed martensite grain (2.4 mrd) differs from that representative for the non-fractured sample. The two planes $(1\,0\,1)_{\alpha'}$ and $(1\,1\,0)_{\alpha'}$ intersecting along the normal direction rotate around ND towards the planes with the maximum shear stresses due to the composite load (p_{m1} and p_{m2} in Fig. 15b). As a result, the first plane deviates by 15° from the sample cross-section, and the normal of the second forms an angle of 45° with
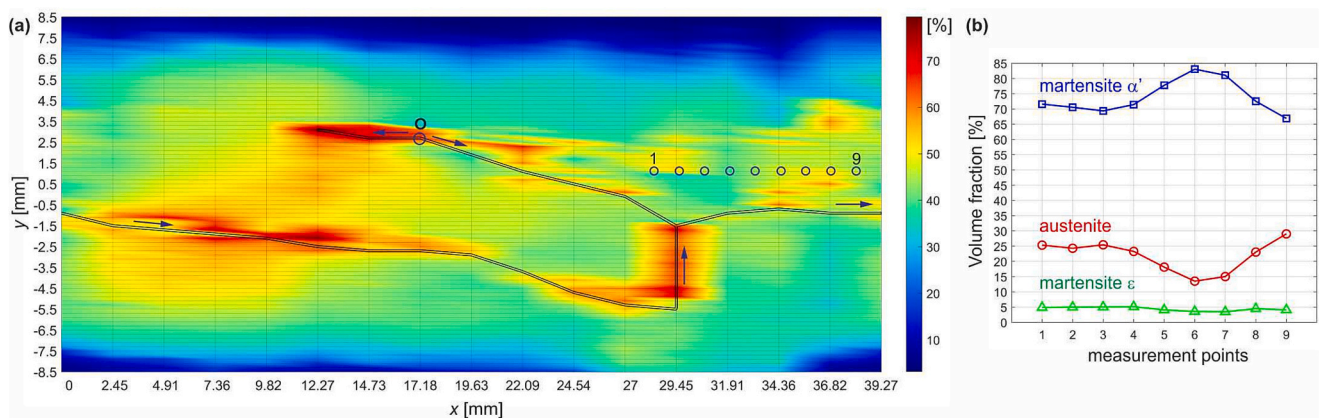
the metal strip between the short crack and the long crack. This is due to the enhanced level of the plastic strains between the crack branches for advanced part of the deformation process. In addition to the global identification of the martensite α' distribution, the phase composition at

Fig. 14. (a) Martensite α' volume fraction determined with the use of feritscope, presented in the unfolded specimen surface. The crack path is marked with black lines. The axis y is parallel to the sample axis and $y = 0$ is at the gauge length center. (b) Volume fractions of the component phases measured by synchrotron XRD in points 1 to 9 along the fracture.
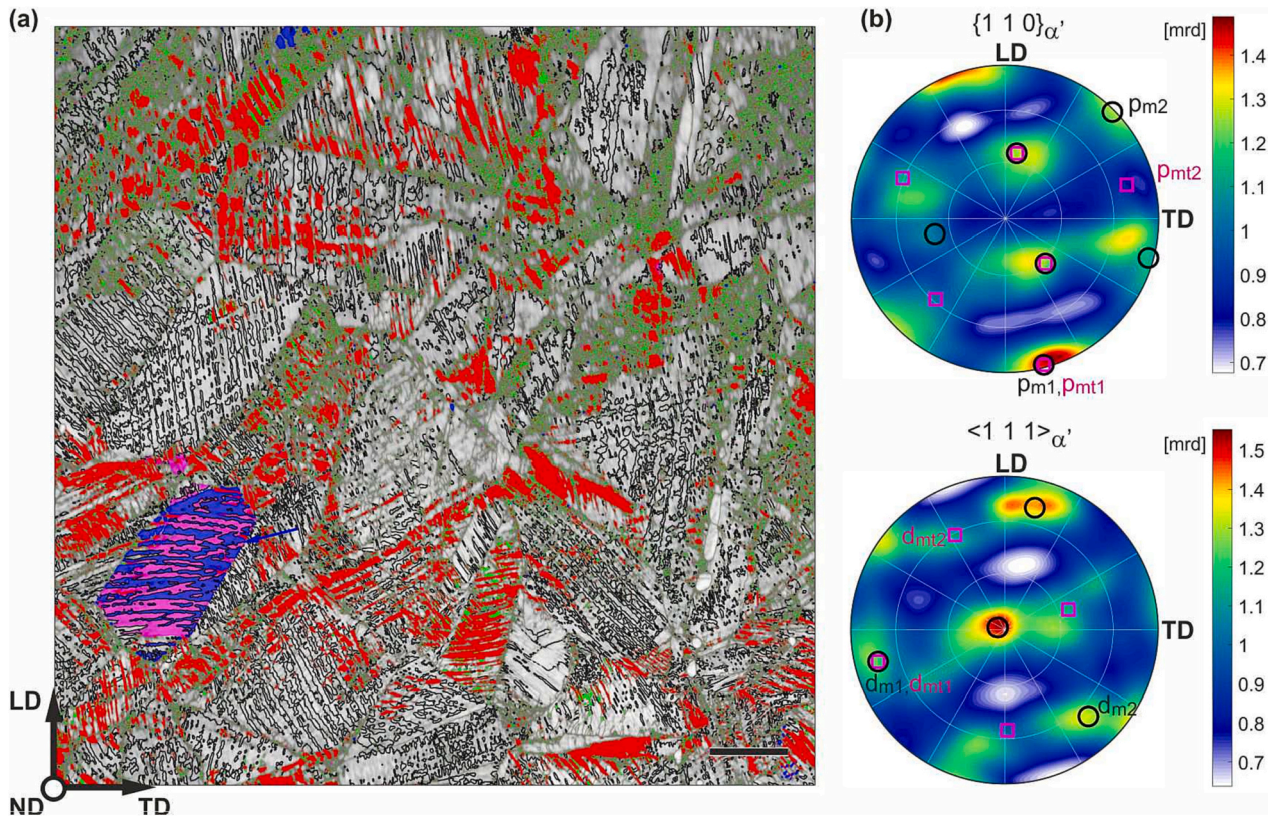
Fig. 15. (a) Microstructure at point 4 adjacent to the macrocrack. Image quality map of martensite α' with austenite (red) and martensite ε (green). Martensite α' twin boundaries are marked with black thick lines, martensite α' grains with the highly preferred orientation according to synchrotron measurements is distinguished in blue and its twin in magenta. The planes p_{m1} and p_{mt1} key for phase transformation are indicated by blue arrow. Scale bar: 10 μm (b) PDF for $\{1\ 1\ 0\}_{\alpha'}$ and $\langle 1\ 1\ 1 \rangle_{\alpha'}$ obtained by synchrotron XRD. Martensite α' orientation with the highest frequency and its twin are marked with black circles and magenta squares, respectively.

respect to TD. Like the non-fractured sample, the shear in the plane $(1\ 0\ 1)_{\alpha'}$ containing the invariant fiber during torsion is preferred. The use of the second plane p_{m2} for phase transformation is difficult due to the significant angle by which it deviates from the plane of maximum shear stresses. Thus, the preferred martensite grain is accompanied by a twin whose plane $(1\ -1\ 0)_{\alpha'}$ is closer to the longitudinal plane and, at the same time, to the plane of maximum shear stresses (p_{mt2} in Fig. 15b). This process is analogous to that found in the non-fractured sample (Fig. 9) and and leads to the martensite cross-growth under the complex load. Thus, when the content of the secondary phase is dominant, the martensite texture becomes more pronounced, less determined by torsion, and more influenced by tension.

The highly preferred martensite α' grain with an accompanying twin is illustrated in the EBSD image. There are clearly visible shear planes, deviated from the cross-section so as to reach the plane of the maximum shear stresses generated by the complex load. They constitute some of twin boundaries (p_{mt1}). There are also differently oriented boundary planes $\{1\ 1\ 0\}_{\alpha'}$, common to the matrix and the twin, formed during the coherent growth of both grains (comp. Fig. 15b). The obtained result illustrating the preferred martensite grain system detected in the XRD synchrotron studies reveals that the martensite cross-growth mechanism induced by two shear systems due to the complex load generates coherent microstructure.

Separately generated regions of martensite join keeping specific, low-energy boundaries with the austenite. As in the case of the first specimen, which was not ruptured, the Pitsch disorientation most often occurs, it is accompanied by the Kurdjumov–Sachs one, and the Nishiyama-Wassermann relationship is relatively rare.

7. Numerical simulations versus experimental data

Numerical analysis has been performed by modelling imperfect thin-walled cylindrical shell, subjected to the combined loads comprising traction and torsion. The analysis has been carried out for the shell corresponding to the tested sample, made of grade 304 austenitic stainless steel. Two cases were studied: the initially cylindrical shell without the macrocrack, and the same shell with the macrocrack initiated at the experimentally identified location. In both cases the original geometry of the shell was modified by imposing an imperfection corresponding to the instability mode of $n = 3$ (in the circumferential direction) (see Fig. 16).

Such a mode has been experimentally identified when performing the tests of cylindrical samples subjected to torsion and traction in liquid helium (4.2 K). Thus, the analysis comprises the shear stresses corresponding to torsion, and the normal stresses corresponding to traction and to flexure due to the initial imperfection. Generally, the numerical analysis has been performed by using triple nonlinearity: the physical nonlinearity (the elastic–plastic model with hardening comprising the finite strains), the geometrical nonlinearity associated with the imperfection imposed on the initial shape, and the XFEM analysis including the macro-crack evolution (fracture). The numerical study of the shell without fracture was regarded as the reference case, for comparison with the shell containing the macrocrack.

7.1. Deformation of the cylindrical shell without fracture – reference case

The reference analysis has been performed without fracture. It consisted in the nonlinear deformation analysis, leading to identification of
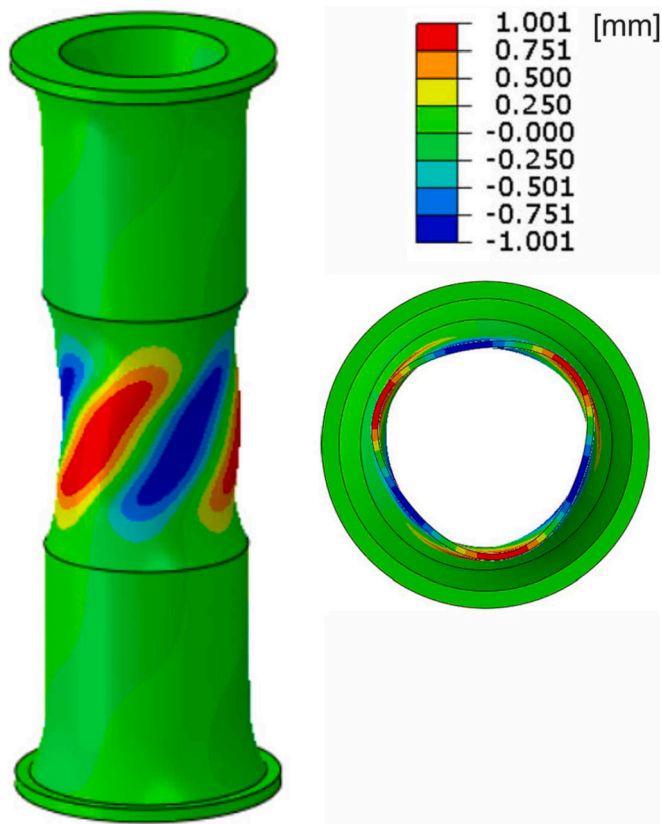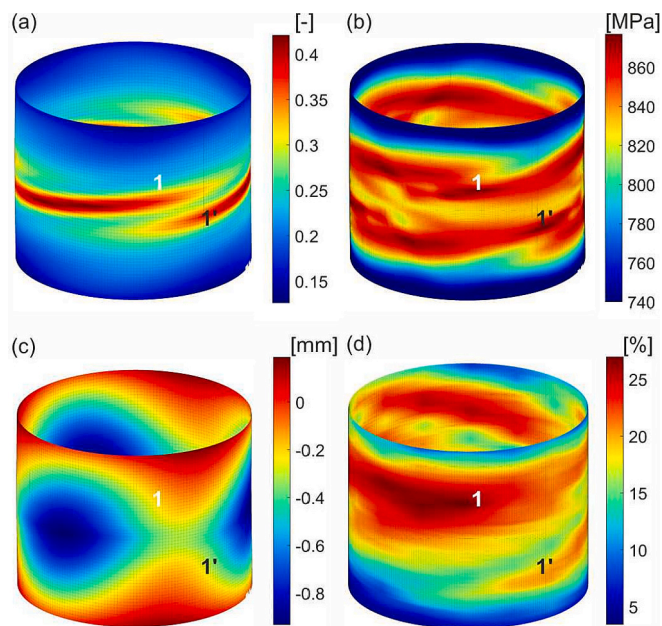
Fig. 16. Instability mode in the shell sample $n = 3$.

the stress and the strain fields. The amplitude of the shape imperfection ($n = 3$) was equal to 0.05 mm.

In order to analyze the fcc-bcc phase transformation, distributions of the plastic strain intensity as well as of the maximum shear stress have been computed. The maps of these quantities are presented on the

Fig. 17. Comparison of numerical results with the experiment (a) map of the plastic strain intensity, (b) distribution of maximum shear stresses (c) field of the radial component of displacement (d) experimental volume fraction of martensite.

cylindrical part of the sample surface (Fig. 17).

The comparison with the martensite α' distribution identified by the feritscope shows that the phase transformation is initiated in the areas of the highest shear stresses on the slope of the buckling fold (point 1 in Fig. 17) and and continues into the well-formed depression according to the increasing plastic strain intensity. The experimentally recorded deformation of the sample differs from that obtained numerically. Its main component is the form of loss of stability, and the narrowing along the sample gauge length is uniform. The FEM model predicts strong strain localization in the center of the gauge section. This leads to the concentration of tensile stresses that reduce the maximum shear stresses. This effect does not occur in the experiment. The maximum shear stresses in the center of the buckling wells reach considerable values due to the presence of the compressive stresses. Thus, the development of martensite α' from the slope to the interior of the depression is conditioned both by the maximum shear stresses and the intensity of plastic deformation.

7.2. Deformation of the cylindrical shell with fracture – evolution of the macro-crack

The main numerical analysis includes the initiation and the propagation of the macro-crack. The macro-crack has been initiated at the location identified directly within the fractured specimen (Fig. 14). It is worth pointing out, that - again - the measured amplitude of the shape imperfection has been imposed in order to stay close to the realistic fracture conditions. The initial macro-crack crosses 2–3 elements in order to trigger sufficient stress concentration for its further evolution. The macro-crack propagation occurs in the circumferential direction, simultaneously at its both extremities. However, in the "leading" direction the propagation is much faster, and the fracture goes all around the circumference of the specimen. Finally, the process ends up with creation of a material strip separating both "short" and "leading" branches of the macro-crack. The whole process is accompanied by strong localization of the plastic strains, which constitute one of the factors inducing fcc-bcc phase transformation. A of secondary phase (martensite α') at the stage preceding sample opening is shown in Fig. 18. It has been obtained in the postprocessor, on the basis of the plastic strain intensity.

Here again, the numerically obtained map of the volume fraction of secondary phase has been compared with the experimentally identified distribution of martensite α'. The correlation of the macro-crack trajectory, and the volume fraction of secondary phase in the vicinity of the macro-crack, is illustrated in Fig. 19. The main effects visible in the tested sample were correctly mapped in the numerical model. Due to the limitation of the FEM method, the different stages of the complex load path were compared. The experimental result depicts the state of the sample after rupture, while the FEM model captures the situation when both macro-crack tips reach the same generator (meridian). Continuation of the simulation in the range of large displacements shows that the lower branch of the macrocrack propagates towards the upper one, heading to junction. Moreover, the degree of phase transformation in the region separated by the fractures is higher. It is worth noting that, in the final stage of the test, the considered region undergoes strong shear. Analysis of the non-ruptured sample showed that the shear stresses were an important factor controlling the phase transformation (Section 4). Thus, the experimentally identified higher martensite α' content in the area between the fractures also results from the participation of significant shear stresses, which is not taken into account in the FEM model.

8. Discussion

Simultaneous torsion and tension of thin-walled cylindrical specimens leads to the loss of stability. The resulting folds and wells of buckling constitute bending forms that differentiate the areas with the
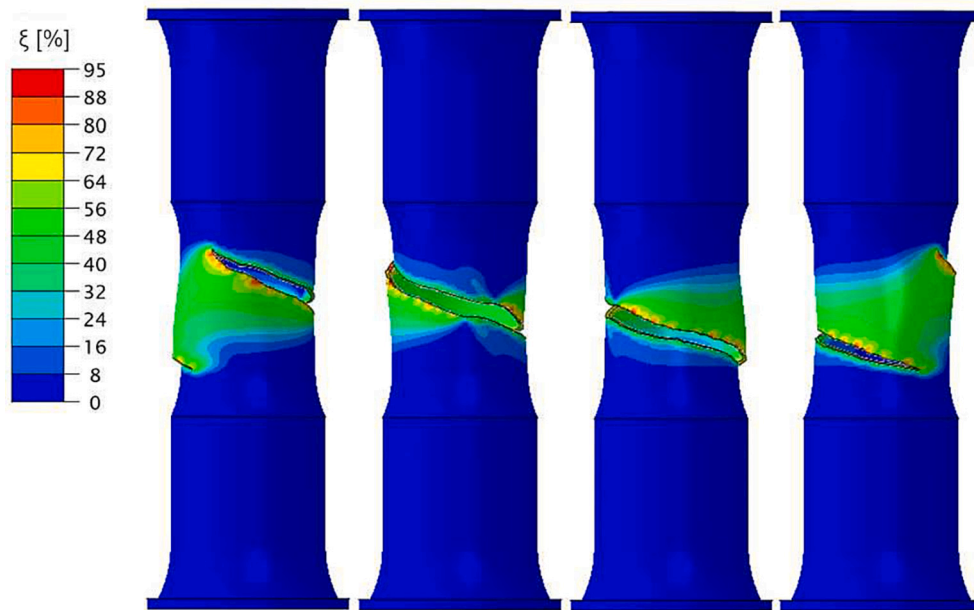
Fig. 18. Map of the volume fraction of martensite α' for the sample with fracture.
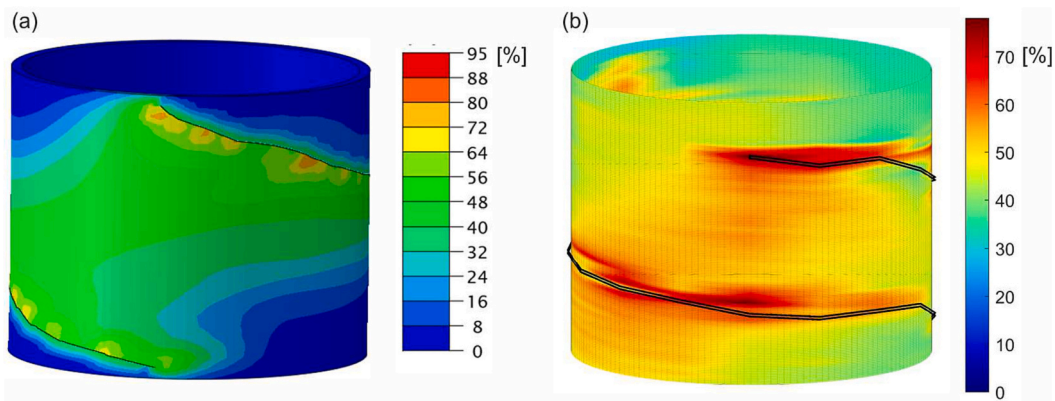

Fig. 19. Distribution of the volume fraction of martensite α' in the gauge section of the fractured sample according to (a) FEM model and (b) feritscope measurement.

highest shear stresses and plastic strain intensities. The former locate on the slopes of the elevations, while the latter in the center of the depressions. The natural separation of regions dominated by different factors controlling the phase transformation allowed to determine the influence of each of them on the formation of the new phase – martensite α'. Ferritoscopic measurements coupled with identification of the sample surface topography with the use of non-contact profilometer show that the maxima of the martensite α' content are located in the slopes of the folds. The phase transformation continues towards the center of the buckling wells, where the martensite α' volume fraction also reaches considerable values. The obtained results indicate that shear stresses play a key role. In the areas where they reach the highest values, the phase transformation is initiated and the fast increase of martensite α' occurs. The secondary phase distribution related to the sample surface geometry reveals that the plastic strain intensity is a weakly correlated factor. It does not decide where the transformation is to be activated, but controls its further course. As a result, the martensite α' fields develop towards the interior of the buckling wells, where the plastic strain intensity reaches its maximum values. The detailed study of the distributions of both factors controlling the phase change is enabled by the simulation of the complex load process with the use of the FEM method. The obtained results clearly confirm the previously detected relationships of maximum shear stresses and the plastic strain intensity with the initiation and growth in martensite α' fields. The complex load test is ended with the formation of a macro-crack. The fracture initiates at the top of the gauge section and develops in accordance with and opposite to the torque. One of the causes of bidirectional propagation is the buckling fold, which hinders the circumferential run of the macrocrack according to the applied torsional moment. The slope of the elevation undergoes stiffening due to the increased content of the harder secondary phase. As a result, apart from the main branch of the fracture, which overcomes the buckling fold, there is a second branch with the opposite direction, which, after a short propagation path, is stopped by a massive phase transformation of up to 100%. The second, more clearly shaped buckling fold, in a similar way as the first, one blocks the development of the macrocrack. As a result, the lower part of fracture meets the upper one, which leads to the sample rupture. The XFEM simulation recreated the macrocrack trajectory with high accuracy. Numerical calculations have shown that a zone with considerable plastic strain intensity is formed between the upper and the lower branch of the macrocrack. According to the experimentally determined kinetics of the phase transformations, 50% of martensite α' content corresponds to it. Ferritoscopic measurements exhibit a higher value of 60%. The difference is due to the fact that the area under consideration is subjected to strong shear, while the

kinetics of transformation is based solely on the plastic strain intensity.

EBSD studies have revealed that a secondary phase with a specific microstructure is formed during torsion combined with tension at the temperature of liquid helium. The first component of load is of key importance. The torsion induces a particular deformation which leaves the material fiber with the transverse direction belonging to the cylinder wall invariant. The characteristic fiber lies in one of the two mutually perpendicular planes of maximum shear stresses. Synchrotron and EBSD studies reveal that this system is reflected in the cross-lamellar morphology of the resulting martensite α'. The conducted analysis shows a clear preference for the plane containing the invariant fiber, perpendicular to the sample axis. These conditions enable the phase transformation according to the Kurdjumov–Sachs or Pitsch path. It was found that the martensite grain, formed in such a way, twins. As a result, the subsequent one arises, which develops along the second available plane of maximum shear stresses. The martensite cross-growth mechanism based on twinning leads to a coherent microstructure at an advanced stage of the phase transformation, exceeding 80%. This time, however, a system of planes is used, rotated around the direction normal to the outer surface, so as to reach the maximum shear stresses generated by the complex load. This is demonstrated by both local EBSD and global synchrotron studies. The resulting coherent martensite has the ability to block propagating cracks and deflect their paths, which was confirmed by the characteristic distribution of the secondary phase uncovered in the fractured sample.

9. Conclusions

The microstructure evolution and its coupling with the fracture process of AISI 304 steel subjected to complex loads at the temperature of liquid helium were investigated. The conducted experimental research and theoretical analysis reveal the key importance of the torsional moment. Contrary to the tensile force, it generates shear stresses along which the material fibers remain invariant. Synchrotron XRD studies show that planes perpendicular to the specimen axis, containing these special directions, become the preferred site for the phase transition. The initiated martensite growth continues in the cross-arranged grains joined to the primary ones by twin boundaries. This regularity was registered in the EBSD images, which shows that the system of mutually perpendicular maximum shear stresses generated by torsion is mapped in the form of a coherent structure of martensite α'.

The mechanism of twin-based cross-growth leads to the formation of compact martensite α' fields at later stages of loading. As a result, the new phase effectively deflects the propagating fracture and blocks its development. The macrocrack trajectory and the secondary phase distribution were reconstructed with high accuracy in the XFEM simulations.

The essential role of shear stresses is also shown by feritoscopic investigations combined with profilometric studies. The highest volume fracture of martensite α' occurs in the regions where the stresses reach the greatest values. Thus, the phase transformation kinetics based on the intensity of plastic strains, giving correct results for tension, should be modified in the case of complex loads so as to include shear stresses.

Declaration of Competing Interest

The authors declare that they have no known competing financial interests or personal relationships that could have appeared to influence the work reported in this paper.

Data availability

Data will be made available on request.

References

[1] D.T. Read, R.P. Reed, Fracture and Strength Properties of Selected Austenitic Stainless Steels at Cryogenic Temperatures, Cryogenics 21 (1981) 415–417.

[2] N.J. Simon, R.P. Reed, Strength and Toughness of AISI 304 and 316 at 4 K,J, Nucl. Matter. 141–143 (1986) 44–48.

[3] B. Skoczeń, J. Bielski, J. Tabin, Multiaxial constitutive model of discontinuous plastic flow at cryogenic temperatures, Int. J. Plast. 55 (2014) 198–218.

[4] M. Sitko, B. Skoczeń, A. Wróblewski, FCC-BCC phase transformation in rectangular beams subjected to plastic straining at cryogenic temperatures, Int. J. Mech. Sci. 52 (7) (2010) 993–1007.

[5] G.S. Sun, L.X. Du, J. Hu, H. Xie, H.Y. Wu, R.D.K. Misra, Ultrahigh strength nano/ultrafine-grained 304 stainless steel through three-stage cold rolling and annealing treatment, Mater. Charact. 110 (2015) 228–235.

[6] G.V.S. Kumar, K.R. Mangipudi, G.V.S. Sastry, L.K. Singh, S. Dhanasekaran, K. Sivaprasad, textitExcellent Combination of Tensile ductility and strength due to nanotwinning and a biamodal structure in cryorolled austenitic stainless steel, Sci. Rep. 10 (1) (2020) 1–9.

[7] K.P. Staudhammer, E. Murr, S.S. Hecker, Nucleation and evolution of strain-induced martensitic (b.c.c.) embryos and substructure in stainless steel: a transmission electron microscope study, Acta Metall. 31 (1983) 267–274.

[8] K. Nalepka, B. Skoczeń, M. Ciepielowska, R. Schmidt, J. Tabin, E. Schmidt, W. Zwolińska-Faryj, R. Chulist, Phase transformation in 316L austenitic steel induced by fracture at cryogenic temperatures: Experiment and modelling, Materials 14 (2021) 127.

[9] X.S. Yang, S. Sun, T.Y. Zhang, The mechanism of bcc α' nucleation in single hcp ε laths in the fcc $\gamma \rightarrow$ hcp $\epsilon \rightarrow$ bcc α' martensitic phase transformation, Acta Mater. 95 (2015) 264–273.

[10] A.J. Bogers, W.G. Burgers, Partial dislocations on the {110} planes in the B.C.C. lattice andthe transition of the F.C.C. into the B.C.C. lattice, Acta Metall 12 (1964) 255.

[11] G.B. Olson, M. Cohen, A perspective on martensitic nucleation, Ann. Rev. Mater. Sci. 11 (1982) 1–30.

[12] L. Bracke, L. Kestens, J. Penning, Transformation mechanism of α'-martensite in an austenitic Fe–Mn–C–N alloy, Scripta Mater. 57 (2007) 385–388.

[13] Y.F. Shen, X.X. Li, X. Sun, Y.D. Wang, L. Zuo, Twinning and martensite in a 304 austenitic stainless steel, Mater. Sci. Eng., A 552 (2012) 514–522.

[14] P.M. Ahmedabadi, V. Kain, A. Agrawal, Modelling kinetics of strain-induced martensite transformation during plastic deformation of austenitic stainless steel, Mater. Des. 109 (2016) 466–475.

[15] John S. Aristeidakis, Gregory N. Haidemenopoulos, Constitutive and transformation kinetics modeling ε-α'-Martensite and mechanical twinning in steels containing austenite, Acta Mater. 228 (2022), 117757.

[16] M. Zecevic, M.V. Upadhyay, E. Polatidis, T. Panzner, H. Van Swygenhoven, M. Knezevic, A crystallographic extension to the Olson-Cohen model for predicting strain path dependence of martensitic transformation, Acta Mater. 166 (2019) 386–401.

[17] P. Debye, Zur Theorie der spezifischen Wärmen, Ann. Phys. 344 (1912) 789–839.

[18] S.W. Van Sciver, Helium Cryogenics, Springer Science, New York, 2012, p. 470.

[19] B. Obst, A. Nyilas, Experimental evidence on the dislocation mechanism of serrated yielding in f.c.c. metals and alloys at low temperatures, Mater. Sci. Eng.: A 137 (1991) 141–150.

[20] V.V. Pustovalov, Serrated deformation of metals and alloys at low temperatures (Review), Low Temp. Phys. 34 (2008) 683–723.

[21] J. Tabin, B. Skoczen, J. Bielski, Strain localization during discontinuous plastic flow at extremely low temperatures, Int. J. Solids Struct. 97–98 (2016) 593–612.

[22] J. Tabin, B. Skoczen, J. Bielski, Discontinuous plastic flow coupled with strain induced fcc–bcc phase transformation at extremely low temperatures, Mech. Mater. 129 (2019) 23–40.

[23] G.B. Olson, M. Cohen, Kinetics of strain-induced martensitic nucleation, Metall. Trans. 6A (1975) 791–795.

[24] C. Garion, B. Skoczeń, Modeling of plastic strain induced martensitic transformation for cryogenic applications, J. Appl. Mech. 69 (2002) 755–762.

[25] R. Ortwein, Constitutive model of graded micro-structure obtained via strain induced phase transformation. PhD Thesis (CERN-THESIS-2015-084), 2015.

[26] J. Talonen, P. Aspegren, H. Hanninen, Comparison of different methods for measuring strain induced α'-martensite content in austenitic steels, Mater. Sci. Technol. 20 (12) (2004) 1506–1512.

[27] A. Glage, A. Weidner, H. Biermann, Effect of austenite stability on the low cycle fatigue behavior and microstructure of high alloyed metastable austenitic cast TRIP steels, Proc. Eng. 2 (2009) 2085–2094.

[28] R. Chulist, P. Czaja, On the role of atomic shuffling in the 4O, 4M and 8M martensite structures in Ni-Mn-Sn single crystal, Scripta Mater. 189 (2020) 106.

[29] A. Wojcik, R. Chulist, P. Czaja, M. Kowalczyk, P. Zackiewicz, N. Schell, W. Maziarz, Evolution of microstructure and crystallographic texture of Ni-Mn-Ga melt-spun ribbons exhibiting 1.15% magnetic field-induced strain, Acta Mater. 219 (2021), 117237.

[30] C. Randau, U. Garbe, H.-G. Brokmeier, StressTextureCalculator: a software tool to extract texture, strain and microstructure information from area-detector measurements, J. Appl. Crystallogr. 44 (2011) 641.

[31] F. Bachmann, R. Hielscher, H. Schaeben, Texture Analysis with MTEX - Free and Open Source Software Toolbox, Solid State Phenom. 160 (2010) 63–68.

[32] ABAQUS, Version 6.14 User's Manual, Dassault Systèmes Simulia Corp.; Providence, RI, USA, 2014.

[33] S. Das, J.J.R. Cheng, D.W. Murray, Prediction of fracture in wrinkled energy pipelines subjected to cyclic deformations, Int. J. Offshore Polar Eng. 17 (2007) 205–212.

[34] S.M. Adeeb, D.J. Horsley, A numerical procedure to establish a safe working pressure during excavation of a pipeline in a rock ditch, Int. J. Press. Vessel. Pip. 83 (2006) 488–497.

[35] Y. Bai, T. Wierzbicki, Application of extended Mohr-Coulomb criterion to ductile fracture, Int. J. Fract. 161 (2010) 1.

[36] M. Paredes, V. Grolleau, T. Wierzbicki, On ductile fracture of 316L stainless steels at room and cryogenic temperature level: An engineering approach to determine material parameters, Materialia. ISSN: 2589-1529 10 (2020), 100624.

[37] Z. Mei, J.W. Morris, Influence of deformation-induced martensite on fatigue crack propagation in 304-type steels, Metall. Mater. Trans. A 21 (1990) 3137–3152.

[38] N. Baffie, J. Stolarz, T. Magnin, Influence of strain-induced martensitic transformation on fatigue short crack behaviour in an austenitic stainless steel, Matériaux Tech. 5–6 (2000) 57–64.

[39] P.T. Purtscher, R.P. Walsh, R.P. Reed, Fracture behaviour of 316LN alloy in uniaxial tension at cryogenic temperatures, Adv. Cryog. Eng. Mater. 34 (1988) 379–386.

[40] R.P. Reed, R.P. Walsh, Tensile strain rate effect in liquid helium, Adv. Cryog. Eng. Mater. 34 (1988) 199–208.